Experimental Verification of Inverse Analysis of Turbidity Currents from Their Deposits by Machine Learning Technique

Zhirong Cai[1] and Hajime Naruse[1]

[1]Kyoto University

November 28, 2022

Abstract

Despite the importance of turbidity currents in environmental and resource geology, their flow conditions and mechanism are not well understood. To resolve this issue, a new method for the inverse analysis of turbidity current using deep learning neural network (DNN) was proposed. This research aims at verifying and calibrating this method using artificial and flume experiment datasets. The forward model based on the shallow water equation was employed in this study to produce artificial datasets of turbidite deposits. DNN was applied to two hundred artificial datasets and two sets of experiment data. As a result of inversion by DNN, spatial distributions of grain size and thickness of experimental turbidites were reconstructed accurately. With regard to hydraulic conditions, the flow heights were reasonably estimated, and sediment concentrations reconstructed were reasonable except for regions where the values measured in experiments were extremely low. Flow duration also showed reasonable reconstructed values. In contrast to the other values, there was a large discrepancy between the measured and reconstructed values of flow velocity. The reason for this discrepancy in velocity may be attributed to inaccuracy in closure functions employed in the forward model. Future application to actual data of natural scale turbidite is anticipated.

Experimental Verification of Inverse Analysis of Turbidity Currents from Their Deposits by Machine Learning Technique

Zhirong Cai[1]*, **Hajime Naruse**[1]

[1]Kyoto University

Key Points:

- Deep Learning Neural Network
- Turbidite
- Flume Experiment

*Kyoto, Japan

Corresponding author: Zhirong Cai, cai.zhirong.64w@kyoto-u.jp

Abstract

Despite the importance of turbidity currents in environmental and resource geology, their flow conditions and mechanism are not well understood. To resolve this issue, a new method for the inverse analysis of turbidity current using deep learning neural network (DNN) was proposed. This research aims at verifying and calibrating this method using artificial and flume experiment datasets. The forward model based on the shallow water equation was employed in this study to produce artificial datasets of turbidite deposits. DNN was applied to two hundred artificial datasets and two sets of experiment data. As a result of inversion by DNN, spatial distributions of grain size and thickness of experimental turbidites were reconstructed accurately. With regard to hydraulic conditions, the flow heights were reasonably estimated, and sediment concentrations reconstructed were reasonable except for regions where the values measured in experiments were extremely low. Flow duration also showed reasonable reconstructed values. In contrast to the other values, there was a large discrepancy between the measured and reconstructed values of flow velocity. The reason for this discrepancy in velocity may be attributed to inaccuracy in closure functions employed in the forward model. Future application to actual data of natural scale turbidite is anticipated.

1 introduction

A turbidity current is a process of sediment transport into subaqueous environments such as deep lakes and ocean (Daly, 1936; Johnson, 1939). The deposits of turbidity currents are called turbidites, which are often characterized by graded bedding and their sedimentary succession called the Bouma sequence (e.g., Kuenen & Migliorini, 1950; Bouma, 1962; Talling et al., 2012). Turbidite deposits have been an active area of study due to its close association with petroleum resources and its role in the destruction of sea-floor equipment, such as the submarine cables (Weimer & Slatt, 2007; Talling et al., 2015). Also, turbidites are often deposited as a result of tsunami triggered turbidity currents (Arai et al., 2013), so that they are potentially useful for estimating recurrence interval of geohazards.

To understand characteristics of turbidites and their implications, it is essential to study the flow behavior of turbidity currents (Talling et al., 2007). However, knowledge in this area remains limited due to difficulties in the direct observation of turbidity currents. A few in-situ measurements were made (e.g., Xu et al., 2004; Vangriesheim et al., 2009; Arai et al., 2013; Paull et al., 2018), but hydraulic conditions measured, such as sediment concentration and flow velocity, were unclear due to the destructive nature and unpredictable occurrences of turbidity currents (Naruse & Olariu, 2008; Falcini et al., 2009; Lesshafft & Marquet, 2010; Talling et al., 2015). Hence, inverse analysis that reconstructs the flow conditions of turbidity currents from their deposits is crucial for estimating the conditions of flows in natural environments.

Prior to this research, inverse analysis of turbidity currents was conducted by Baas et al. (2000), where flow velocity was reconstructed through analyses of the sedimentary structures of turbidites. The results gave an estimation of the instantaneous hydraulic conditions of the flow, but did not provide a reconstruction of its spatio-temporal evolution. In contrast to the reconstruction of flow conditions based on sedimentary structures, inverse analysis methods based on numerical models provided more detailed insights to the inner structure of flow and the evolution of flow over time (e.g., Falcini et al., 2009; Lesshafft & Marquet, 2010; Parkinson et al., 2017). However, the method proposed by Falcini et al. (2009) assumed the steady flow conditions and was simplified for obtaining analytical solutions, preventing it from accurately illustrating the flow mechanism of unsteady turbidity currents that can produce normally graded bedding. As a result, this method could not be used to analyzed graded beds. Other studies employed the optimization method where hydraulic parameters are estimated by optimizing the input parameters of numerical models so that the resulting calculations fit the observed data from turbidites (Lesshafft & Marquet, 2010). This method can provide a relatively good reconstruction of the hydraulic conditions of turbidity currents, but is extremely high in calculation load, making it impossible to be applied to natural scale turbidite, which typically runs over tens to hundreds of kilometers and flows continuously for several hours (Talling et al., 2015). Optimization using the adjoint approach proposed by Parkinson et al. (2017) solved the problem of high calculation load, but the reconstructed values were very low inaccuracy.

In order to resolve the issues mentioned above, Naruse and Nakao (2017) developed a new method for inverse analysis of turbidite deposits using deep learning neural network (DNN). DNN is a computational scheme that can work as a universal function approximator (Liang & Srikant, 2016). In the past, it was applied to problems such as landslide susceptibility analyses (Pradhan et al., 2010) and identification of lithology from well log data (Rogers et al., 1992), where the logical relationship between the observed data and values that aimed to be predicted were explored. It was proven in Naruse and Nakao (2017) that DNN is capable of exploring the relationship between deposit profile of turbidite and the initial flow conditions of the turbidity current that deposits it. When using DNN as a method of inversion for turbidity currents, training datasets and verification datasets were first produced using a forward model. Training

datasets were inputted into DNN during a process called training. During training, DNN explores the functional relationship between the deposits and the initial flow conditions. After training, DNN becomes capable of making estimations on turbidite data it had not seen before. Although application of the method to artificial datasets was successful, it has yet to be tested with actual turbidite data.

In this study, we verified DNN's ability to perform inverse analysis of turbidity currents by applying it to data collected from actual turbidites deposited in flume experiments. In each flume experiment, a turbidity current was generated under a controlled condition. Conditions including flow duration and initial hydraulic conditions can be set manually, and measurements of these parameters can also be conducted easily during the flow. Thus, rather than data measured in nature, flume experiment works better as a first step for verifying the accuracy of DNN for the inverse analysis on turbidity currents.

Here, we implemented the forward model and DNN for inversion. Trained DNN was first tested with artificial data of experimental scale turbidity currents. It was then tested with data sampled from flume experiments. The initial flow conditions were reconstructed from deposit profiles sampled. The reconstructed flow conditions were also fed into the forward model and the spatio-temporal evolution of the flow was reconstructed. The hydraulic conditions during the flow and the eventual grain-size distribution of the deposits reconstructed were also compared with the measured values.

2 Forward Model

2.1 Governing Equations

Forward model implemented in this study is a layer-averaged model based on Kostic and Parker (2006). It is expanded to account for the transport and deposition of non-uniform grain size distribution that is discretized to multiple grain-size classes in Nakao and Naruse (2017) (Figure 1). The five governing equations are as follows:

$$\frac{\partial H}{\partial t} + U\frac{\partial H}{\partial x} = e_{\mathrm{w}}U - H\frac{\partial U}{\partial x} \tag{1}$$

$$\frac{\partial U}{\partial t} + U\frac{\partial U}{\partial x} = RC_{\mathrm{T}}g(S - \frac{\partial H}{\partial x}) - \frac{1}{2}gHR\frac{\partial C_{\mathrm{T}}}{\partial x} - \frac{U^2}{H}(c_{\mathrm{f}} - e_{\mathrm{w}}) \tag{2}$$

$$\frac{\partial C_i}{\partial t} + U\frac{\partial C_i}{\partial x} = \frac{w_i}{H}(F_i e_{\mathrm{s}i} - r_{\mathrm{o}}C_i) - \frac{e_{\mathrm{w}}C_i U}{H} \tag{3}$$

$$\frac{\partial \eta_i}{\partial t} = \frac{w_i}{1-\lambda_{\mathrm{p}}}(r_{\mathrm{o}}C_i - e_{\mathrm{s}i}F_i) \tag{4}$$

$$\frac{\partial F_i}{\partial t} + \frac{F_i}{L_{\mathrm{a}}}\frac{\partial \eta_{\mathrm{T}}}{\partial t} = \frac{w_i}{L_{\mathrm{a}}(1-\lambda_{\mathrm{p}})}(r_{\mathrm{o}}C_i - e_{\mathrm{s}i}F_i) \tag{5}$$

where the equations represent fluid mass conservation (equation 1), momentum conservation (equation 2), sediment mass conservation (equation 3), mass conservation in bed (Exner's equation) (equation 4) and sediment mass conservation in active layer (equation 5), respectively (Nakao & Naruse, 2017).

Parameter x is the streamwise distance and t is time. Parameters H, U and C_i are the flow height, the layer-averaged velocity and the layer-averaged volumetric concentration of suspended sediment of the ith grain-size class, respectively. Parameter C_{T} denotes the layer-averaged total concentration of suspended sediment ($C_{\mathrm{T}} = \sum C_i$), and g is gravitational acceleration. Parameter S and c_{f} are the slope gradient and the friction coefficient. Parameters R, the submerged specific density of sediment, w_i, the settling velocity of a sediment particle of the ith grain-size class, and λ_{p}, the porosity of bed sediment, describe the sediment properties. Parameter η_i is the volume per

unit area of bed sediment of the ith grain-size class and η_{T} is the sum of all η_i ($\eta_{\mathrm{T}} = \sum \eta_i$). Parameter L_{a}, the active layer thickness, and F_i, the volume fraction of the ith grain-size class in active layer, describes the structure of active layer. Parameter $e_{\mathrm{s}i}$, e_{w} and r_{o} are the entrainment rate of sediment of the ith grain-size class into suspension, the entrainment rate of ambient water to flow, and the ratio of near-bed suspended sediment concentration to the layer-averaged concentration of suspended sediment (Figure 1). The closure equations of the parameters mentioned are described in Section 2.2.

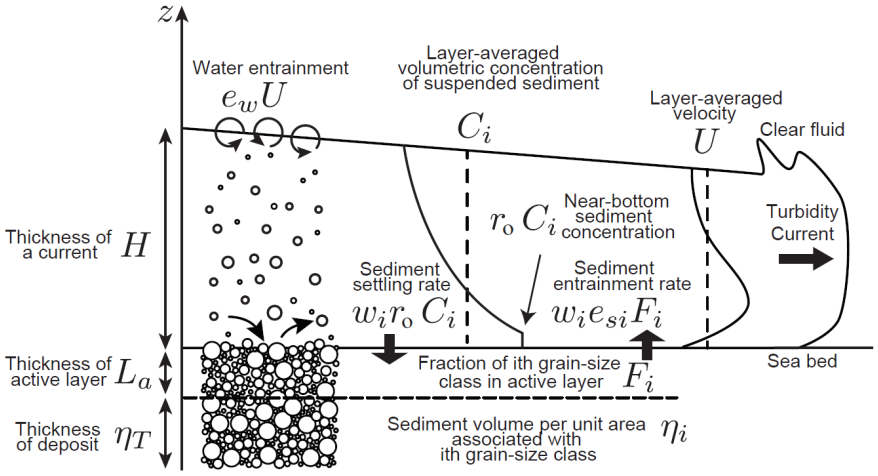

Figure 1. Schematic diagram of processes considered in the forward model from (Nakao & Naruse, 2017).

2.2 Closure Equations

Empirical formulations from previous studies are adapted to close the governing equations. In this study, friction coefficient c_{f} is assumed to be a constant value. The particle settling velocity w_i for each grain-size class with a representative grain diameter D_i is calculated using the relation from Dietrich (1982), which can be expressed as follows:

$$w_i = R_{\mathrm{f}i}\sqrt{RgD_i} \tag{6}$$

$$R_{\mathrm{f}i} = \exp(-b_1 + b_2\log(Re_{\mathrm{p}i}) - b_3(\log(Re_{\mathrm{p}i}))^2 - b_4(\log(Re_{\mathrm{p}i}))^3 + b_5(\log(Re_{\mathrm{p}i}))^4) \tag{7}$$

$$Re_{\mathrm{p}i} = \frac{\sqrt{RgD_i}D_i}{\nu} \tag{8}$$

where b_1, b_2, b_3, b_4 and b_5 are 2.891394, 0.95296, 0.056835, 0,000245 and 0.000245, respectively. e_{w} is calculated by the empirical formula from Fukushima et al. (1985) as follows:

$$e_{\mathrm{w}} = \frac{0.00153}{0.0204 + (RC_{\mathrm{T}}H/U^2)} \tag{9}$$

The entrainment coefficient of sediment e_{s} is calculated using the empirical relation from Wright and Parker (2004):

$$e_{\mathrm{s}i} = \frac{aZ^5}{1 + (a/0.03)Z^5} \tag{10}$$

$$Z = \alpha_1 \frac{u_*}{w_i} Re_{\mathrm{p}}^{\alpha_2} S_{\mathrm{f}}^{0.08} \tag{11}$$

where shear velocity u_* and friction slope S_f are calculated as follows:

$$u_* = \sqrt{c_\mathrm{f}}U \tag{12}$$

$$S_\mathrm{f} = \frac{c_\mathrm{f}U^2}{RgC_\mathrm{T}H} \tag{13}$$

and the constants α_1 and α_2 are 0.586 and 1.23 respectively if $Re_\mathrm{p} \leq 2.36$, and are 1.0 and 0.6 respectively if $Re_\mathrm{p} > 2.36$. Kinematic viscosity of water ν is calculated as follows:

$$\nu = \mu/\rho \tag{14}$$

where ρ is the density of water. μ is the dynamic viscosity of water. Experimentally determined values for μ at different temperature (Rumble, 2018) are used in the calculation of ν.

2.3 Implementation of Forward Model

In this study, the constrained interpolation profile (CIP) method (Yabe et al., 2001) was used for the integration of the partial differential equations 1, 2 and 3. In order to stabilize the calculation, artificial viscosity was applied with the scheme of Jameson et al. (1981), in which the parameter κ was set to 0.25. The two-step Adams-Bashforth method was used to solve ordinary differential equations 4 and 5. The interval of spatial grids Δx was set to 0.05 m and the time step Δt was set to 0.01 second. S was set according to the range of flume deposits chosen for calculation, which is specified in Section 5. Initial value of S was 10 % for all grids.

Dirichlet boundary condition was used for the upstream boundary, and Neumann boundary condition was used for the downstream boundary. The upper boundary of calculation was set with constant flow conditions, including the initial flow height H_0, the initial flow velocity U_0, the initial total volumetric concentration of sediment $C_{\mathrm{T},0}$, and the initial volumetric concentration of each grain-size class $C_{i,0}$. Parameter $F_{i,0}$, the initial volume fraction of the ith grain-size class in active layer, were all set to 0.25 for all grain-size classes. The downstream boundary was set to the same value as the grid adjacent to the lower boundary toward the upstream direction. Other than the upstream boundary, all flow parameters including flow height H, velocity U, concentration C_i were initialized to zero.

The number of grain-size classes and representative grain diameters are determined based on the grain size distribution of experiments performed and are specified in Section 5.1. Temperature was set to 20.0 °C for numerical simulations. R was set to 0.5 for all grain-size classes. c_f was set to 0.002. r_o was 0.5. λ_p was set to 0.4. L_a was set to 0.003 m. g was 9.81 m/s^2. ρ was 1000.0 kg/m^3.

3 Inverse Analysis by Deep Learning Nerual Network

In this method, initial flow conditions of turbidity currents are reconstructed from its turbidite deposits. DNN first explores the functional relationship between the initial flow conditions of turbidity currents and the resulting turbidite deposits in a process called training. After the training process, it is applied to new turbidite datasets for inverse analysis. In preparation for training, artificial training datasets are produced using the forward model. During the training process, training datasets are fed into DNN. DNN examines the datasets and adjusts to make good estimation of the initial flow conditions from the deposit profiles. After training, DNN, which is now capable of predicting the initial flow conditions of new turbidites based on the functional relationship it found, is tested with independent artificial datasets that are also produced from the forward model and with flume experiment data.

3.1 Production of Training Data

A training dataset is a combination of randomly generated initial flow conditions at the upstream boundary of the flow and a matching deposit profile calculated by the forward model. A program in Python was written to generate sets of initial flow conditions. Each set of flow conditions generated consists of an initial flow velocity U_0, an initial flow height H_0, a flow duration T_d, and the initial concentrations of each grain-size class $C_{i,0}$. Other variables, such as slope, are set to constant values.

Table 1. Range of initial flow conditions generated for the production of training datasets.

Parameter	Minimum	Maximum
H_0 (m)	0.005	0.3
U_0 (m/s)	0.001	0.3
$C_{i,0}$	0.0001	0.02
T_d (s)	1080	120

Forward model calculates the deposit profile of turbidite from the randomly generated initial flow conditions. The deposit profile is calculated as volume per unit area for each grain-size class at a total of 80 locations within a 4 m range streamwise. Each data point is 0.05 m away from its neighboring points. Ranges of randomly generated initial flow conditions are shown in Table 1. In this study, 11800 training datasets were produced and used for training and 200 test cases were used for verification of DNN. These test artificial datasets were produced independently from the training datasets.

3.2 Structure of Deep Learning Neural Network

The type of neural network used in this case is the fully connected neural network, which consists of an input layer, several hidden layers, and an output layer. Each layer consists of a number of nodes. Each node connects with every node in the adjacent layers (Figure 2A). In the input layer, the nodes hold the values of the deposit profile, i.e. the volume-per-unit-area for all grain-size classes at spatial grids. In the output layer, the nodes hold estimates of the values we seek to reconstruct, which in this case are the initial flow conditions U_0, H_0, $C_{i,0}$ and the flow duration T_d. The activation function used in this case is ReLU, which is one of the most common activation functions used for DNN and is proven to perform calculations at a higher speed than other activation functions (Krizhevsky et al., 2012).

Before training, weight coefficients are set to random values. As the training process begins, values of deposit profile from the training datasets are inputted to the nodes at the input layer. These values propagate through the hidden layers of DNN and estimates of initial flow conditions are outputted at the output layer. At this point of training, DNN is yet to adapt its internal variables to the functional relationship between turbidite deposits and initial flow conditions, so that the initial estimates are expected to be largely off from the actual values of the deposit profile inputted. In order to explore this functional relationship, a loss function is used to evaluate the accuracy of the estimated values. Loss function used in this case is the mean squared error function, which is considered as one of the best functions for regression (Wang & Bovik, 2009). The gradient of the loss function is calculated back to the hidden layers of DNN through a process called backpropagation (Nielsen, 2015; Schmidhuber, 2015), so that the internal values are optimized toward minimizing the difference between the estimated and the actual values. This process is repeated for

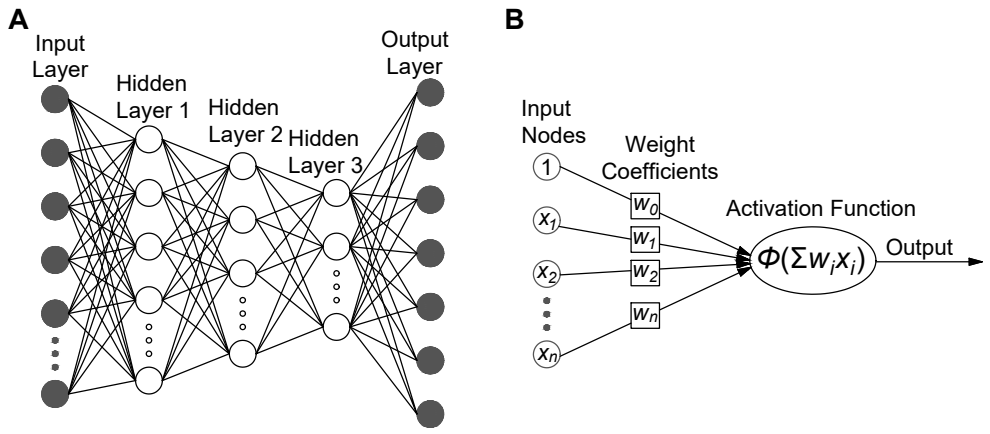

Figure 2. Schematic diagrams of DNN. A. Overall structure of DNN. B. Concept of weight coefficient and activation function.

every epoch of calculation. An epoch is a cycle of calculation in DNN that involves one forward pass and one backpropagation of all training data.

Optimization of the result of loss function is performed by an optimization algorithm within DNN. The optimization algorithm used in this study is the stochastic gradient descent (SGD), which drastically reduces the amount of calculation involved in training without sacrificing accuracy in comparison to previous algorithms of gradient descent (Bottou, 2010). In this study, Nesterov momentum is employed (Ruder, 2016). Due to difference in the range of initial flow conditions, normalization needs to be applied to training datasets before they are inputted to DNN. In this case, all values are normalized to a value between 0 and 1 for DNN to consider all parameters at equal weight. Hyperparameters including the number of layers, number of nodes at each layer, dropout rate, validation split, learning rate, batch size, epoch, and momentum were adjusted manually. Various combinations were attempted and the best combination of parameters was chosen based on the performance of DNN, which is judged on the basis of the final validation loss.

In this study, DNN was programmed in python using the package Keras 2.2.4. The package Tensorflow 1.14.0 (Abadi et al., 2015) was used for backend calculation. Calculations were conducted using GPU NVIDIA GeForce GTX 1080 Ti.

3.3 Evaluation of Trained DNN Model

When verifying DNN with test artificial datasets (Section 5.1), reconstruction results of each parameter were evaluated using bias (B) and sample standard deviation (s) of residuals. The calculations were conducted using the equations below:

$$B = \frac{\sum x_i}{n} \tag{15}$$

$$s = \sqrt{\frac{\sum (x_i - B)^2}{n-1}} \tag{16}$$

$$\tag{17}$$

where n is the number of test datasets. x_i denotes the residual of the reconstructed value of the specific parameter for ith test dataset. The calculated s and B for reconstructed parameters are shown in Table 4 and Table 5. The value of s of each

reconstructed parameter was compared with a representative value C_v^*, which is the mid-value over the range in which the specific parameter was generated in production of artificial datasets (Table 1). The confidence interval of B was determined using bootstrap resampling method (Davison & Hinkley, 1997). Resampling of B was conducted for 10000 times and the 95% confidence interval (CI) of B was determined.

During verification of DNN using flume experiment data (Section 5.2), the flow parameters at the upstream end of simulation, 1.0 meters from the upstream boundary of the flume, were reconstructed by the inversion method from the measured properties of the deposit profile. The reconstructed parameters were inputted into the forward model so that the flow parameters downstream and the evolution of deposit profile over time were calculated. After the flow simulation reached a steady condition, the calculated flow parameters downstream were compared with the measured values of experimental flow conditions at the locations where the measurement instruments were set. Inversion results of flow conditions of experiments are shown in Table 6 and 7. The deposit profile calculated from the reconstructed flow parameters were also compared with the measured deposit profile that was used for inversion. The comparisons of deposit profile are shown in Figures 6 and 8.

4 Flume Experiments

4.1 Experiment Settings

In this study, flume experiments were conducted in the flume located in the basement of Building No.1 of the Faculty of Science at Yoshida Campus, Kyoto University. The flume was made of acrylic panels and is 4 m in length, 0.12 m in width and 0.5 m in depth. It was submerged in a tank made of glass panels and steel supporting frame that was 5.5 m in length, 2.5 m in width and 1.8 m in depth. Slope of channel floor was changed at a middle point of the flume (1.0 m from the inlet), where the upstream slope a was 0 to 5 degrees and the downstream slope b was set to 5 degrees (Figure 3). Specific values of a are stated in Section 4.3. Sediment was mixed with water in the two mixing tanks before experiment.

During experiment, the mixture of sediment and water was first pumped to the constant head tank, and then released into the flume from the valve at the base of the constant head tank. Flow discharge was regulated by the opening of the flow control valve. The amount of mixture in the constant head tank was kept at a constant level to maintain a stable flow discharge. The damping tank at the downstream end of the flume prevented flow from reflecting back toward the upstream side. A pipe of freshwater supply was placed at the top of the damping tank and a draining pipe was placed at the bottom of the damping tank. The combination of these two pipes kept the level of water in the tank constant and also prevented reflection of flow.

Five experiments were conducted in this research for the purpose of verifying DNN's ability to reconstruct the initial flow conditions from the resulting turbidite deposits. Two experiments were performed using two types of plastic particle (experiments PP1, PP2 (Section 4.3)). One type of plastic particle (polyvinyl chloride) used had a density of 1.45 g/cm^3 and an average grain diameter of 0.120 mm. Another type of plastic particle (Melamine) used had a density of 1.45 g/cm^3 and an average grain diameter of 0.220 mm. Three experiments were performed using a mixture of siliciclastic sand and polyvinyl chloride plastic particle (experiments BS1, BS2, BS3 (Section 4.3)). Siliciclastic sand had a density of 2.65 g/cm^3 and an average grain diameter of 0.250 mm.

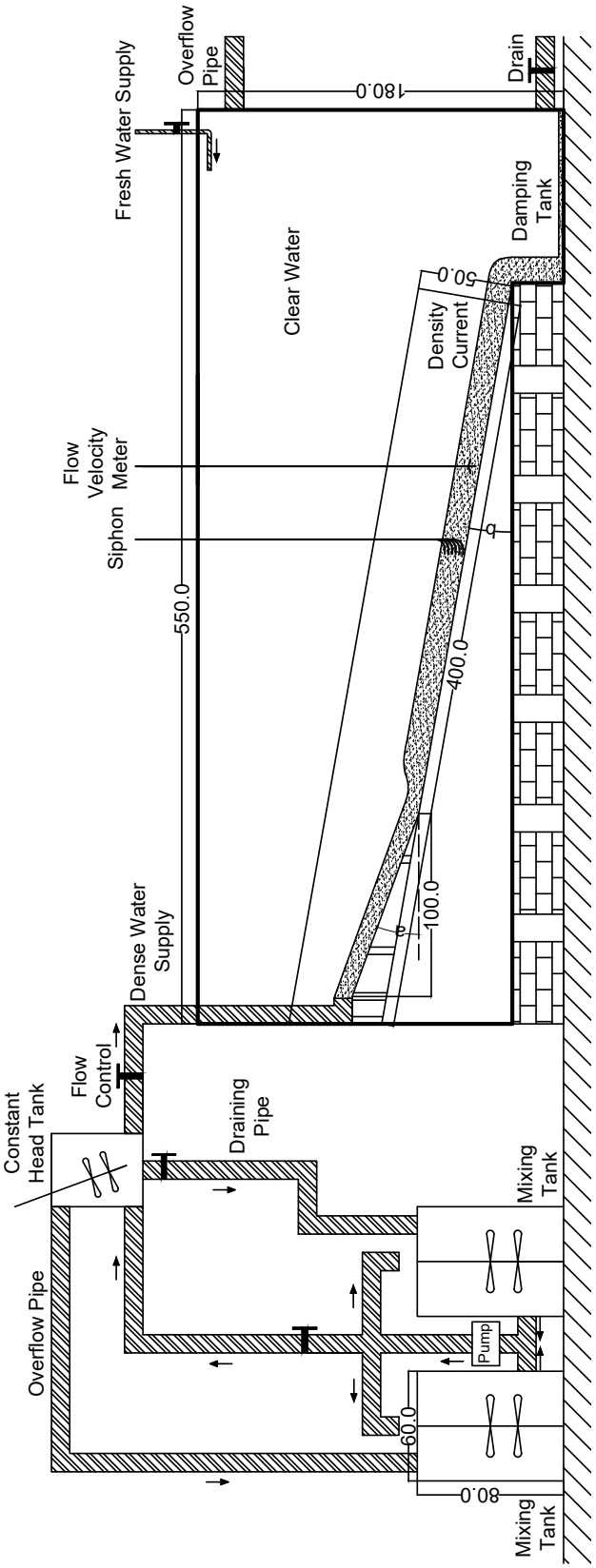

Figure 3. Schematic diagram of flume used for experiment. (All values have unit cm.)

4.2 Measurements and Data Analysis

Before each experiment, tank water temperature was measured using a glass alcohol thermometer. A beaker of the mixture in tank was sampled for measurement of the initial concentration in tank. Flow velocity during experiment was measured with an acoustic Doppler velocity profiler (ADVP; Nortek Vectrino Profiler). The functional range of the ADVP used was $4.0 - 7.0$ cm from the probe. In order to obtain the vertical velocity profile of the flow, an actuator was used to adjust the position of ADVP during experiments.

A siphon with 10 plastic tubes was used to sample the suspended concentration of flow. The tubes were aligned vertically at 1.0 cm interval and were positioned so that samples were collected at 0.0 to 9.0 cm above bed. Aluminum tubes with an outer diameter of 8.0 mm and an inner diameter of 5.0 mm were attached at the outlets of the tubes to stabilize its position when sampling during experiments. The sampling of siphon was conducted when the flow reached a quasi-equilibrium state. The state of flow was determined by observation of the developing process of the flow. Two single-lens reflex cameras were used to record the experiments. Flow height of the flow was determined based on the video recorded.

After experiments, the flume was left untouched for 1 to 3 days for the suspended sediment to settle. After that, photos were taken from a perpendicular view to the flume, where the lateral view of the deposited sediment could be seen together with a ruler. The height of deposit was determined from the photos. Water was then drained slowly from the tank with a bath pump at a rate of 0.0002333 m^3/s. After water was drained, deposited sediment was sampled at a 20 cm interval starting from the upstream boundary of the flume.

Samples from siphon and tank were first weighted right after collected. After that, samples from deposited sediment and from siphon and tank were dried. Weight of samples from siphon and tank after drying was recorded for the purpose of calculating the concentration of flow and of mixture in tank. Grain size distribution analysis was conducted in a settling tube for all samples. The settling tube used was 1.8 m long. Calculation of grain size distribution was performed using STube (Naruse, 2005). The particle settling velocity was calculated by Gibbs (1974).

Measured grain-size distribution of sediment was discretized to four grain-size classes. For experiments using plastic particle only, representative grain diameter of grain-size classes 1, 2, 3 and 4 were set to be 210 μm, 149 μm, 105 μm and 74.3 μm, respectively. For experiments using mixture of siliciclastic sand and plastic particle, representative grain diameter of grain-size classes 1, 2, 3 and 4 were set to be 297 μm, 210 μm, 149 μm and 105 μm, respectively. Grain size distributions of sand and plastic particle are partially overlapped, so that concentrations of grain-size classes 2 and 3 were each represented by two separate parameters $C_{2,BS,0}$ and $C_{2,PP,0}$, $C_{3,BS,0}$ and $C_{3,PP,0}$, which are the siliciclastic sand and the plastic particle portion in the grain-size classes 2 and 3.

In steady flow conditions, the relationship between layer-averaged flow velocity U, layer-averaged sediment volumetric concentration C, and flow height H is defined as follow (Garcia & Parker, 1993):

$$UCH = \int_a^\infty u_z c_z dz \tag{18}$$

where u_z and c_z are the flow velocity and sediment volumetric concentration at elevation z above bed. The relationship between layer-averaged flow velocity U and the velocity maximum U_m is defined with the following equation (Altinakar et al., 1996):

$$\frac{U_\mathrm{m}}{U} = 1.3 \tag{19}$$

Layer-averaged flow velocity was calculated from the velocity profile measured by ADVP using the relationship described by equation 19. Sediment volumetric concentration were calculated from siphon measurements according to the relationship described by equation 18.

4.3 Experimental Conditions

Experimental conditions for the five runs conducted are shown in Table 2 and Table 3. C_{TT} is the total concentration of sediment in the mixing tank. $C_{1\mathrm{T}}$, $C_{2\mathrm{T}}$, $C_{3\mathrm{T}}$, $C_{4\mathrm{T}}$ are the concentrations of grain-size class 1, 2, 3, and 4, respectively. $C_{2\mathrm{T,BS}}$ and $C_{2\mathrm{T,PP}}$, $C_{3\mathrm{T,BS}}$ and $C_{3\mathrm{T,PP}}$ in Table 3 are the concentrations of the siliciclastic sand portion and the plastic particle portion of grain-size class 2 and 3. Parameter x_{C} is the position of siphon downstream, x_{U} is the position of flow velocity meter downstream and x_{H} is the position where flow height is measured from video taken. Temperature is the measured temperature of clear water in tank before experiment. Slope a (the slope added on top of slope b upstream) of the flume was 26.8 % and slope b (the base slope) was 10 % (Figure 3) for experiments PP1, PP2, BS2, and BS3. For experiment BS1, both Slope a and b were 10 %.

Table 2. Conditions and settings of experiments conducted with two types of plastic particle.

	PP1	PP2
C_{TT}	0.0191	0.0276
$C_{1\mathrm{T}}$	0.0102	0.0160
$C_{2\mathrm{T}}$	0.00713	0.00820
$C_{3\mathrm{T}}$	0.00146	0.00254
$C_{4\mathrm{T}}$	0.000366	0.000817
x_{C} (m)	1.08	2.10
x_{U} (m)	1.46	2.48
x_{H} (m)	1.10	1.10
Temperature (°C)	22.5	17.0

Table 3. Conditions and settings of experiments conducted with a mixture of siliciclastic sand and plastic particle.

	BS1	BS2	BS3
C_{TT}	0.0229	0.0587	0.0140
$C_{1\mathrm{T}}$	0.000626	0.0246	0.000122
$C_{2\mathrm{T,BS}}$	0.00117	0.0101	0.00385
$C_{2\mathrm{T,PP}}$	0.00314	0.00958	0.00251
$C_{3\mathrm{T,BS}}$	0.00136	0.00811	0.00503
$C_{3\mathrm{T,PP}}$	0.00573	0.00424	0.00164
$C_{4\mathrm{T}}$	0.00543	0.00202	0.000846
x_{C} (m)	2.48	2.33	1.85
x_{U} (m)	2.10	2.71	2.23
x_{H} (m)	1.40	1.40	1.40
Temperature (°C)	12.8	9.5	12.2

5 Results

Inverse analysis was applied to deposits within a 2.6 meters range downstream starting at the end of slope a (1 meter from the upstream boundary of the flume). Due to limited size of the flume, slope a was set at a steep angle in all experiments other than BS1 to accelerate the flow. Considering that the region with slope a was largely affected by instabilities from the outlet pipe and is overly steep in comparison to those observed in nature, the region with slope a was excluded from the range of inversion. Thus, artificial training datasets and verification datasets were produced with the upstream boundary set at the end of slope a. Artificial deposits were produced in the calculation domain from the upstream boundary (corresponding to 1.0 m from the outlet pipe in experiments) to 2.6 m (3.6 m in the experiments), and were used for training and verification. The actual numerical simulation was conducted for 4.0 meters, 1.4 meters longer than the actual range used for inversion, so that the influence of the boundary conditions at the downstream end was minimized.

With regard to the values of hyperparameters used during the training process, dropout rate, validation split and momentum for DNN were 0.5, 0.2, and 0.9, respectively. Learning rate was set to 0.01, batch size to 32, number of layers to 5, number of nodes each layer to 2000, and epochs to 15000. With this settling the eventual validation loss was 0.0031 when applied to plastic particle only training datasets and 0.0020 when applied to siliciclastic sand plastic particle mixture training datasets. Figures 4A and 5A show that overlearning did not occur, since no deviation is observed between values of loss function in training and validation datasets.

5.1 Verification with Artificial Datasets

Here the results of verification with artificial test datasets are exhibited. Results of parameters reconstructed by DNN are shown in Figures 4 and 5. The flow conditions reconstructed include flow velocity U_0, flow depth H_0, sediment concentrations at the upstream end, and flow duration T_d. Verification was conducted separately for artificial datasets of experiments using plastic particle only and artificial datasets of experiments using a mixture of siliciclastic sand and plastic particle. The results are described in the following sections 5.1.1 and 5.1.2, respectively.

5.1.1 Verification of the inverse model for experiments using plastic particle only with test artificial datasets

As an overall trend, reconstructed values mostly coincide with the original values, with a few values scattering further away from the line of perfect match (the diagonal solid line) (Figure 4B, C, D, E, F, G, H). A greater degree of scattering is observed for U_0 (Figure 4D). Flow duration T_d shows a tendency of underestimation (Figure 4B). The range of misfit ($2s$) show relatively good value for T_d, H_0, $C_{2,0}$, $C_{3,0}$ and $C_{4,0}$, which have $2s/C_v^*$ values under 20%. U_0 and $C_{1,0}$ is slightly more scattered but have $2s/C_v^*$ values under 23% (Table 4). 95% confidence interval (CI) of B include zero except for T_d and $C_{2,0}$, where the CI range lies below zero for T_d and above zero for $C_{2,0}$.

Table 4. Sample standard deviation and bias of the inversion result of artificial datasets for plastic particle only experiments.

Parameters	s	C_v^*	$2s/C_v^*$	B	CI of B
U_0 (m/s)	0.0168	0.1505	0.223	-0.000950	(-0.00330, 0.00134)
H_0 (m)	0.0141	0.1525	0.185	0.0000279	(-0.00193, 0.00196)
T_d (s)	53.5	600	0.178	-34.0	(-41.7, -26.7)
$C_{1,0}$	0.00104	0.01005	0.207	-0.0000243	(-0.000164, 0.000126)
$C_{2,0}$	0.000913	0.1005	0.0182	0.000150	(0.0000263, 0.000275)
$C_{3,0}$	0.000985	0.1005	0.0196	0.000131	(-0.00000208, 0.000273)
$C_{4,0}$	0.000869	0.1005	0.173	0.0000445	(-0.0000794, 0.000162)

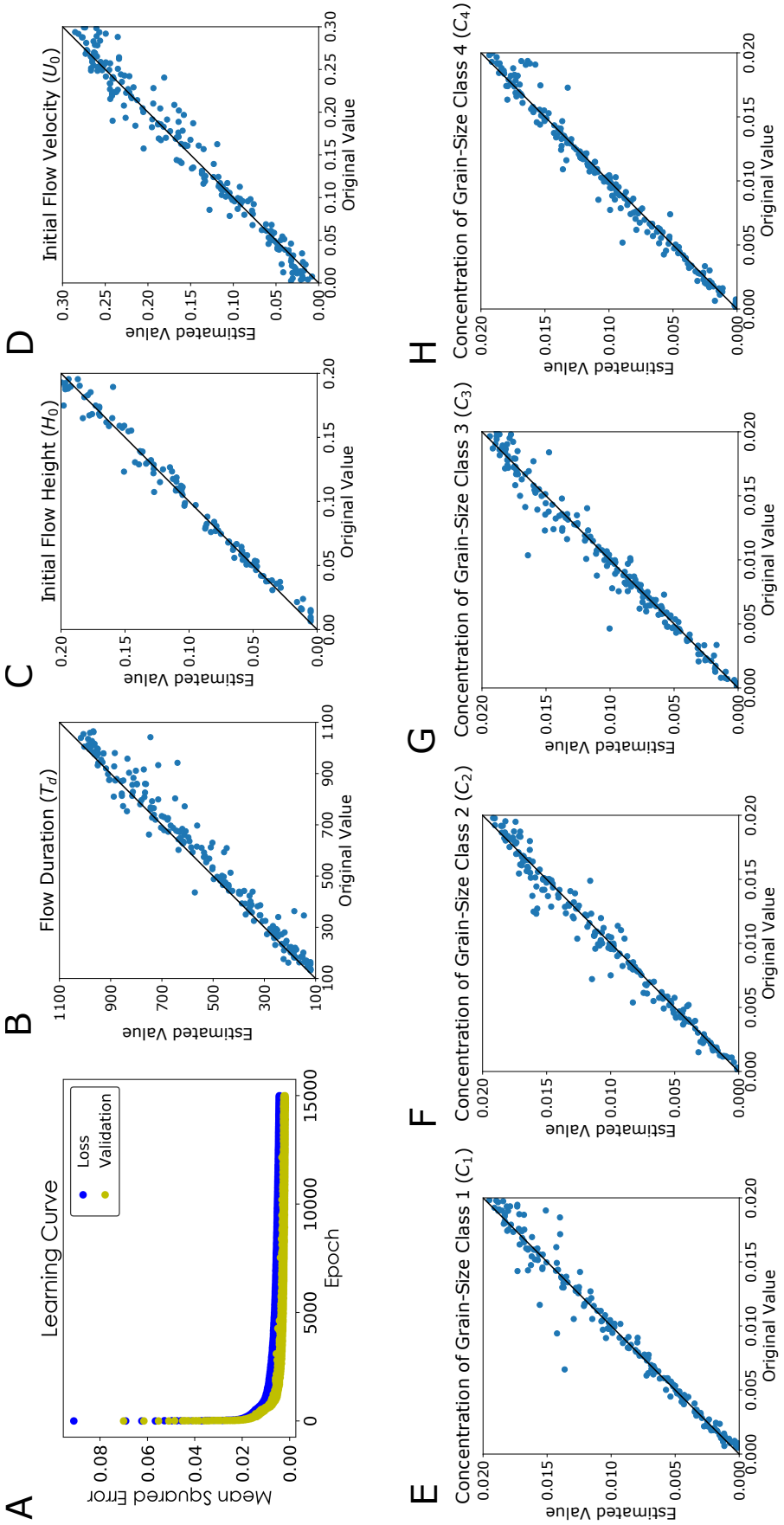

Figure 4. Result of verification with independent artificial datasets for plastic particle only experiments. The black diagonal line in each graph is where values on the x-axis (the true values) equals to the values on the y-axis (the estimated values). If a point lies on this, the reconstructed value matches the true value perfectly. A. Learning curve. B. Estimates of T_d. C. Estimates of H_0. D. Estimates of U_0. E. Estimates of $C_{1,0}$. F. Estimates of $C_{2,0}$. G. Estimates of $C_{3,0}$. H. Estimates of $C_{4,0}$.

5.1.2 Verification of the inverse model for experiments using siliciclastic sand and plastic particle with test artificial datasets

As an overall trend, the reconstructed values and the true flow parameters show a good correlation. Reconstructed values show mostly perfect match with the original values, with a few values scattering from the line of perfect match (the diagonal black line) (Figure 5B, C, D, E, F, G, H, I, J). A greater degree of scattering is observed for U_0 and a tendency of overestimation is observed (Figure 4D). T_d shows a tendency of underestimation (Figure 4B). The range of misfit ($2s$) is good for H_0, $C_{1,0}$, $C_{2,PP,0}$ and $C_{3,PP,0}$, which have $2s/C_v^*$ values under 15%. T_d, $C_{2,PP,0}$, $C_{3,BS,0}$ and $C_{4,0}$ have a moderately good ($2s$), which lie under 18% of their representative values. U_0 is more scattered, having $2s/C_v^*$ value of 28.2% (Table 4). 95% confidence interval of B include zero except for U_0, H_0, T_d, $C_{1,0}$ and $C_{2,PP,0}$, where the CI range lies below zero for T_d and H_0, and above zero for U_0, $C_{1,0}$ and $C_{2,PP,0}$.

Table 5. Sample standard deviation and bias of the inversion result of artificial datasets for siliciclastic sand plastic particle mixture experiments.

Parameters	s	C_v^*	$2s/C_v^*$	B	CI of B
U_0 (m/s)	0.0212	0.1505	0.282	0.00513	(0.00221, 0.00805)
H_0 (m)	0.0110	0.1525	0.144	-0.00293	(-0.00443, -0.00139)
T_d (s)	50.7	600	0.169	-24.8	(-32.3, -18.3)
$C_{1,0}$	0.000631	0.1005	0.0126	0.000185	(0.0000983, 0.000274)
$C_{2,BS,0}$	0.000872	0.1005	0.0174	0.0000783	(-0.0000395, 0.000205)
$C_{2,PP,0}$	0.000740	0.1005	0.0147	0.000124	(0.0000242, 0.000229)
$C_{3,BS,0}$	0.000803	0.1005	0.0160	0.0000846	(-0.0000192, 0.000202)
$C_{3,PP,0}$	0.000724	0.1005	0.0144	0.0000637	(-0.0000341, 0.000168)
$C_{4,0}$	0.000784	0.1005	0.0156	-0.0000873	(-0.000192, 0.0000264)

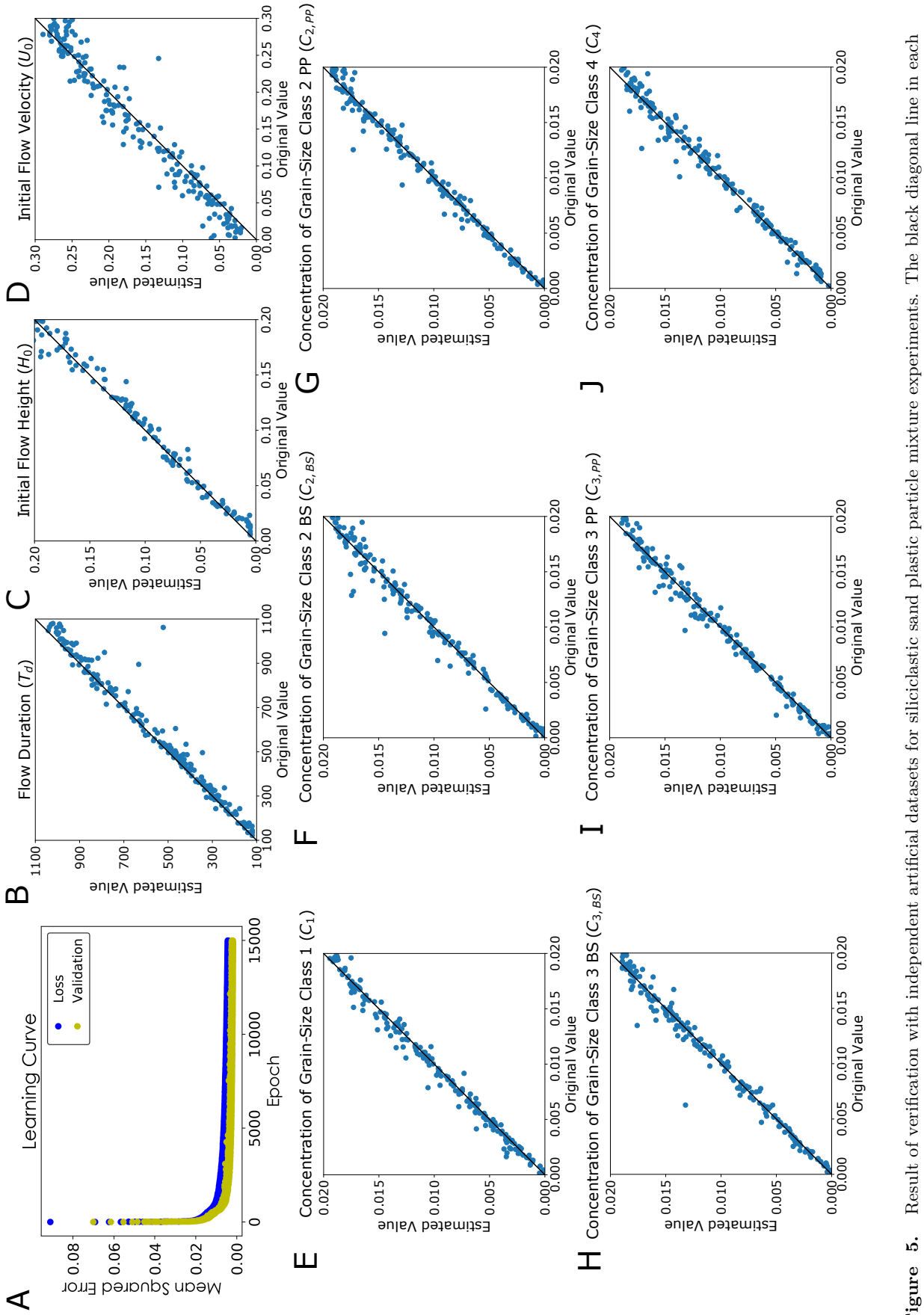

Figure 5. Result of verification with independent artificial datasets for siliciclastic sand plastic particle mixture experiments. The black diagonal line in each graph is where values on the x-axis (the true values) equals to the values on the y-axis (the estimated values). If a point lies on this, the reconstructed value matches the true value perfectly. A. Learning curve. B. Estimates of T_d. C. Estimates of H_0. D. Estimates of U_0. E. Estimates of $C_{1,0}$. F. Estimates of $C_{2,BS,0}$. G. Estimates of $C_{2,PP,0}$. H. Estimates of $C_{3,BS,0}$. I. Estimates of $C_{3,PP,0}$. J. Estimates of $C_{4,0}$.

5.2 Inverse Analysis of Flume Experiment Data

In this section, the deposit profiles and grain size distributions calculated were compared with the actual deposit profiles sampled (Figures 6, 8). Result of flow conditions reconstructed, include flow velocity U_{x_U}, flow height H_{x_H}, sediment concentrations at location x_C downstream and flow duration T_d, were compared with the measured values during experiments (Tables 6 and 7). Inversion results of plastic particle only experiments (PP1, PP2) and experiments using mixture of siliciclastic sand and plastic particle (BS1, BS2, BS3) are described in sections 5.2.1 and 5.2.2.

5.2.1 Experiments using Plastic Particle only (PP1, PP2)

Depositional profiles in these experiments exhibit thinning and fining downstream trends with concave-upward geometry. Reconstructed deposit profiles of the total deposit match closely with the sampled ones for both runs (Figures 6A(1), B(1)). Grain size distribution at 1.4 m and 1.8 m downstream also show good agreement for the reconstructed and measured values for both experiments (Figures 6A(2),(3), B(2),(3)), with PP2 having a slightly better reconstruction than PP1.

The measured and reconstructed values were in good agreement for the flow height H_{x_H} (Figure 7A), which is the flow height H at position x_H downstream when the flow reached a quasi-equilibrium state. Reconstructed H_{x_H} were 0.129 m and 0.156 m for PP1 and PP2, respectively (Table 6). The values matches well with the measured values for PP1 (0.116 m) and PP2 (0.123 m). Reconstructed flow velocities U_{x_U}, which are the velocities U at position x_C (see the positions in Table 2) downstream when the flow reached a quasi-equilibrium state, were 0.136 m/s (PP1) and 0.121 m/s (PP2). The reconstructed values were close to the measured value for PP2 (0.0923 m/s), but had a larger difference for that of PP1 (0.0608 m/s). Reconstructed values of flow duration T_d were 622 s (PP1) and 731 s (PP2), which were lower than the measured values for both PP1 (936 s) and PP2 (966 s) (Figure 7C). Reconstructed values of total concentration $C_{\mathrm{T,x_C}}$ were 0.00579 (PP1) and 0.000370 (PP2), which were the total concentrations C_T at position x_C downstream when the flow reached a quasi-equilibrium state, did not match well with the measured value of $C_{\mathrm{T,x_C}}$ for PP1 (0.000808), but was close to that of PP2 (0.00410). The reconstructed values of each grain-size class is good overall, but large deviation is observed for several reconstructions of concentrations that have very low measured values (Figure 7D)

Table 6. Flow conditions measured and reconstructed for experiments PP1 and PP2. (R.: reconstructed, M.: Measured)

Parameters	PP1 R.	PP1 M.	PP2 R.	PP2 M.
$C_{\mathrm{T,x_C}}$	0.00579	0.000808	0.00370	0.00410
C_{1,x_C}	0.00303	0.0000911	0.000830	0.000612
C_{2,x_C}	0.00180	0.000389	0.00178	0.00224
C_{3,x_C}	0.000868	0.000228	0.000624	0.000944
C_{4,x_C}	0.000100	0.0000999	0.000467	0.000303
H_{x_H} (m)	0.129	0.116	0.156	0.123
U_{x_U} (m/s)	0.136	0.0608	0.121	0.0923
T_d (s)	622	936	731	966

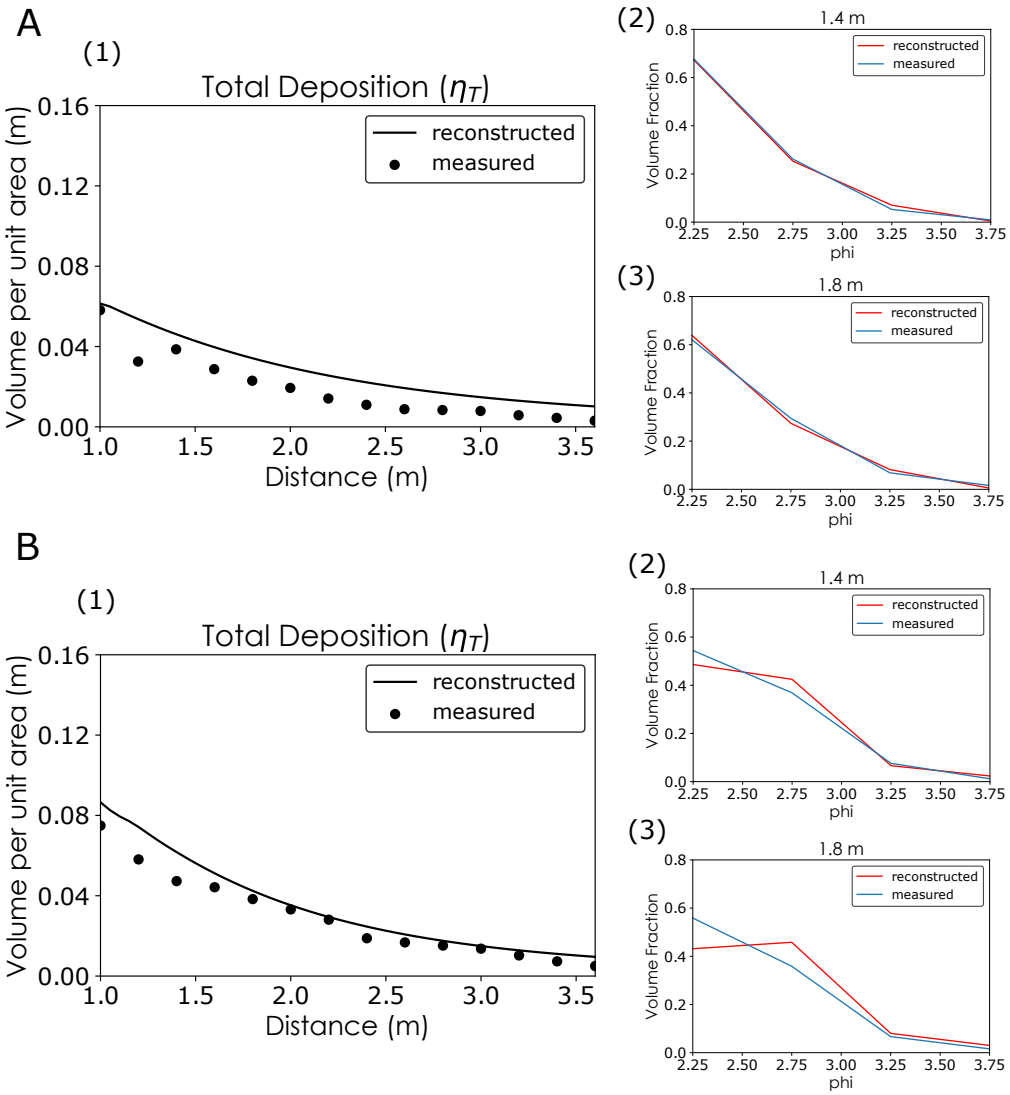

Figure 6. Reconstructed deposit profiles and the sampled deposit data of experiments PP1 and PP2. A. (1) Reconstructed and sampled η_T of PP1. (2) Grain size distribution at 1.4 m downstream. (3) Grain size distribution at 1.8 m downstream. B. (1) Reconstructed and sampled η_T of PP2. (2) Grain size distribution at 1.4 m downstream. (3) Grain size distribution at 1.8 m downstream.

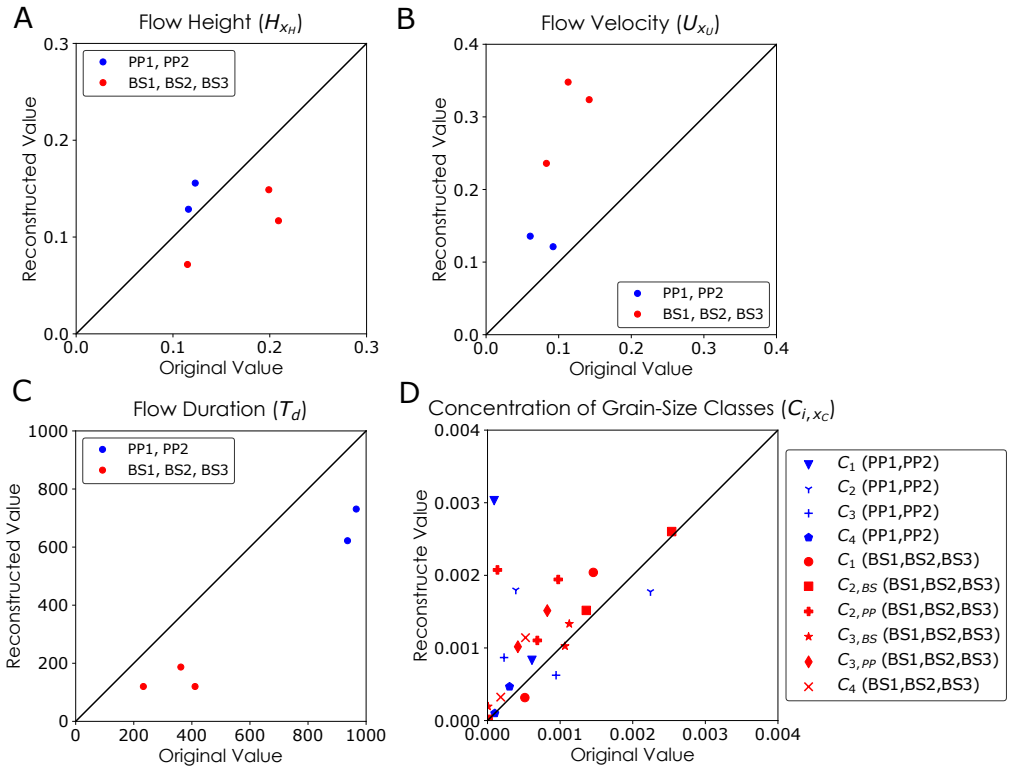

Figure 7. Reconstructed vs measured flow conditions for experiments PP1, PP2, BS1, BS2 and BS3. A. Plot for H_{x_H}. B. Plot for U_{x_U}. C. Plot for T_{d}. D. Plot for C_{i,x_C}.

5.2.2 Experiments using mixture of siliciclastic sand and plastic particle (BS1, BS2, BS3)

Similar to the results in the experiments using plastic particle only, all depositional profiles in these experiments exhibit thinning and fining downstream trends. Turbidite beds deposited in experiments BS2 and BS3 show large concavity in profiles, while the bed in Experiment BS1 shows relatively uniform thickness distribution. Reconstructed deposit profiles of the total deposit match closely with the sampled ones for all three runs (Figures 8A(1), B(1), C(1)). Grain size distribution at 1.3 m and 1.7 m downstream also show good agreement for the reconstructed and measured values for the three experiments (Figures 6A(2),(3), B(2),(3), C(2),(3)).

Reconstructed values of flow height H_{x_H}, which is the flow height H at position x_H (see the positions in Table 3) downstream when the flow reached a quasi-equilibrium state, were 0.0717 m, 0.117 and 0.149 m for BS1, BS2 and BS3, respectively (Table 7). The value is quite close to the measured value for BS1 (0.115 m), but differs for BS2 (0.209 m) and BS3 (0.199 m). Reconstructed flow velocities U_{x_U} were 0.236 m/s (BS1), 0.324 m/s (BS2) and 0.348 m/s (BS3). The reconstructed values did not match well with the measured values 0.0831 m/s (BS1), 0.142 m/s (BS2) and 0.113 m/s (BS3) (Figure 7B). Flow duration T_{d} reconstructed were 120 s (BS1), 187 s (BS2) and 120 s (BS3), which are relatively close to the measured value for BS2 (362 s) and BS3 (233 s), but further off for BS1 (411 s). Reconstructed values of total concentration $C_{\mathrm{T,x_C}}$ were 0.0131 (BS1), 0.00776 (BS2) and 0.00811 (BS3), which matches relatively well for all three experiments BS1 (0.00306), BS2 (0.00532) and BS3 (0.00635). The reconstructed values of each grain-size class is good overall, but large deviation is observed for several reconstructions of concentrations that have very low measured values (Figure 7D).

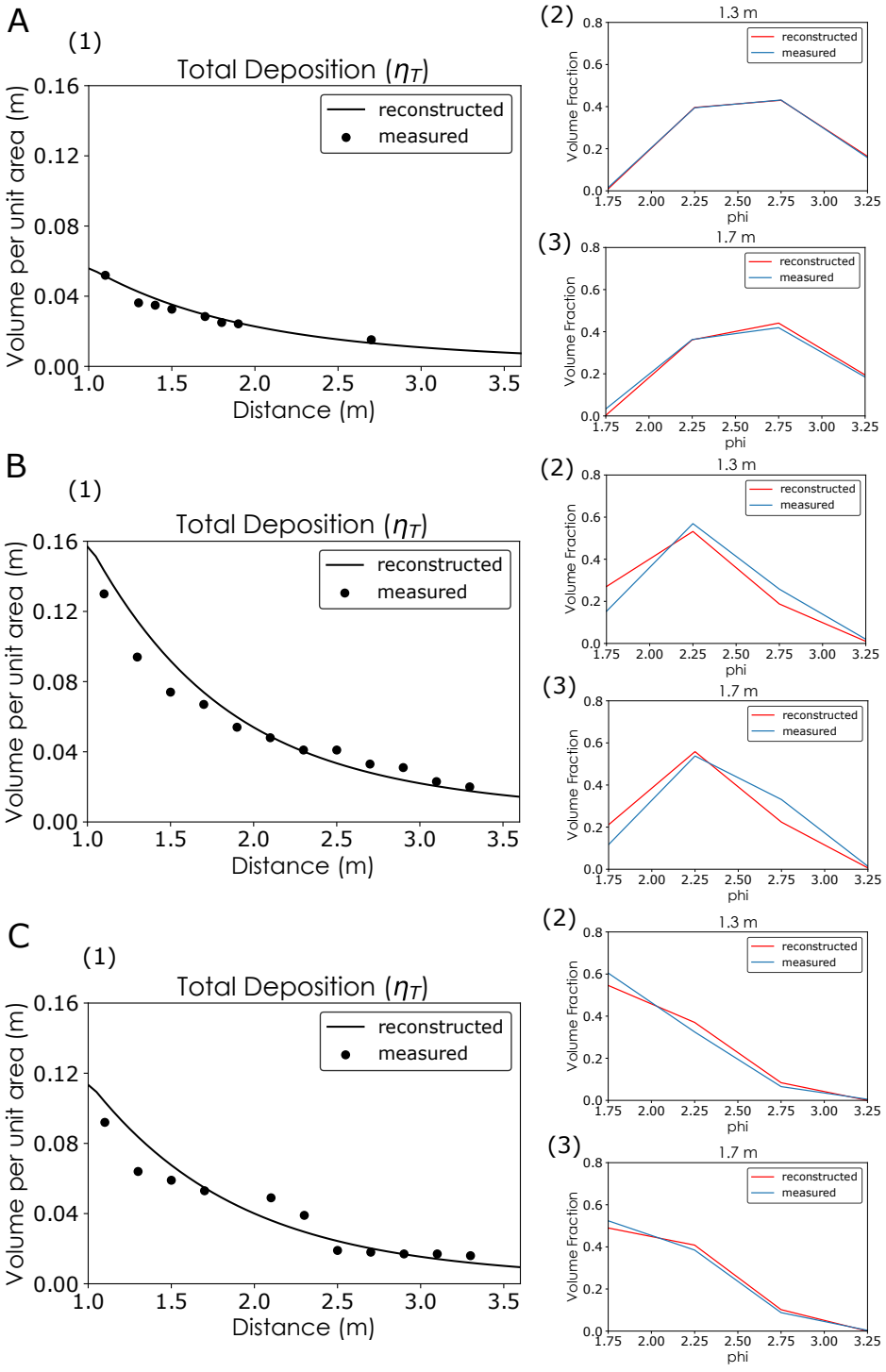

Figure 8. Reconstructed deposit profiles and the sampled deposit data of experiments BS1, BS2 and BS3. A. (1) Reconstructed and sampled η_T of BS1. (2) Grain size distribution at 1.4 m downstream. (3) Grain size distribution at 1.8 m downstream. B. (1) Reconstructed and sampled η_T of BS2. (2) Grain size distribution at 1.4 m downstream. (3) Grain size distribution at 1.8 m downstream. C. (1) Reconstructed and sampled η_T of BS3. (2) Grain size distribution at 1.4 m downstream. (3) Grain size distribution at 1.8 m downstream.

Table 7. Flow conditions measured and reconstructed for experiments BS1, BS2, and BS3. (R.: reconstructed, M.: Measured)

Parameters	BS1 R.	BS1 M.	BS2 R.	BS2 M.	BS3 R.	BS3 M.
$C_{\mathrm{T,x_C}}$	0.0131	0.00306	0.00776	0.00532	0.00811	0.00635
C_{1,x_C}	0.00000101	0.00000466	0.000316	0.000514	0.00204	0.00146
C_{2,BS,x_C}	0.0000167	0.00000905	0.00152	0.00136	0.00260	0.00254
C_{2,PP,x_C}	0.00207	0.000137	0.00194	0.000974	0.00110	0.000686
C_{3,BS,x_C}	0.000194	0.00000751	0.00133	0.00113	0.00103	0.00107
C_{3,PP,x_C}	0.00500	0.00136	0.00151	0.000823	0.00102	0.000418
C_{4,x_C}	0.00578	0.00154	0.00114	0.000523	0.000323	0.000182
H_{x_H} (m)	0.0717	0.115	0.117	0.209	0.149	0.199
U_{x_U} (m/s)	0.236	0.0831	0.324	0.142	0.348	0.113
T_{d} (s)	120	411	187	362	120	233

6 Discussion

6.1 Validation of DNN as an Inversion Method for Turbidity Currents by Artificial Test Datasets

Verification result with artificial datasets proves DNN's ability in reasonably reconstructing the hydraulic conditions of turbidity currents from its turbidite deposits. Reconstruction of initial flow conditions and the flow duration for artificial datasets (Section 5.1.1 and 5.1.2) was good overall judging from the s and B values (Table 4 and 5). The reconstructions of T_{d}, H_0, U_0, $C_{1,0}$, $C_{2,0}$ ($C_{2,BS,0}$ and $C_{2,PP,0}$ for mixture experiments), $C_{3,0}$ ($C_{3,BS,0}$ and $C_{3,PP,0}$ for mixture experiments), and $C_{4,0}$ were high in precision (Table 4 and 5).

Overall, the correlation between the true and the reconstructed values was obvious for all parameters reconstructed. Some scattering was observed for the reconstructed parameters, but most values stayed close within the range of perfect reconstruction. The standard deviation and bias of the parameters reconstructed were all relatively small in comparison to the matching representative values (Table 4 and 5), proving the reconstruction to be high in precision and accuracy. Thus, it can be said that this method is suitable for estimating the paleo-hydraulic conditions of actual turbidity currents.

As described above, most of the reconstructed parameters exhibit no significant bias from the true original conditions. Although reconstructed values of several parameters show statistically significant bias, their deviation is very minor in comparison with the representative values of the parameters (Table 4 and 5). For example, in both experiments using plastic particle only and mixture experiments, the estimation bias B for T_{d} had a negative value and the range of the confidence interval of B was below zero (Table 4 and 5), indicating a tendency of underestimation for T_{d}. However, the bias for T_{d} is only 4.1% (mixture experiments) or 5.6% (plastic particle only) of the representative value of this parameter (600 s).

6.2 Verification of DNN Inversion with Flume Experiment Data

As a result of inversion using DNN, the overall deposit profiles were well reconstructed for all five experiments, and the reconstructed grain size distribution downstream matched with the grain size distribution sampled from experimental deposits

(Figures 6 and 8). DNN as an inverse method tries to find the combination of hydraulic conditions that best produces the deposit profiles inputted. The fact that the reconstructed hydraulic conditions accurately reproduced the deposit profiles used for inverse analysis indicates good performance with the inverse model by DNN.

Also, hydraulic conditions and flow duration reconstructed mostly lay within a reasonable range from the line of perfect reconstruction (Figure 7). Among the reconstructed hydraulic conditions, flow heights H_{x_H} were well reconstructed for all five experiments (Table 6) and 7), and flow durations T_d were reasonably reconstructed but were underestimated for all five experiments as seen also in artificial test datasets. Reconstructed concentration of each grain-size class C_{i,x_C} was largely scattered when the measured values in the experimental flume were very low ($< 0.05\%$). In contrast to other parameters, flow velocities U_{x_U} were largely overestimated for all five experiments.

One potential reason of deviation in reconstructed values is that inverse analysis itself is essentially difficult for turbidity currents. For instance, flow parameters cannot be reconstructed when different combinations of initial conditions produce the exact same deposit profile. However, this is unlikely because flows with a wide variety of initial conditions were tested with artificial datasets and the reconstruction was mostly reasonable, proving DNN's ability to distinguish minor differences in characteristics of deposits. Instead, source of deviation could lie in the process of inverse analysis conducted in this study.

Through analyzing the result of application of DNN to flume experiment data, it was clear that there are three aspects for deviations in the reconstruction of hydraulic conditions: (1) the tendency of deviation within the inverse model, (2) difficulty in measurements during experiments, and (3) inaccuracy within the forward model of turbidity currents employed in this study.

(1) When applying DNN to artificial test datasets, the tendencies of deviation in values reconstructed similar to those observed in the reconstruction of flume experiment datasets were observed (Table 4 and 5). T_d and H_{x_H} reconstructed for flume experiments showed the same tendencies of deviation during reconstruction of artificial test datasets. Thus, deviation in the reconstruction of these two parameters can be considered as a systematic error originating from the internal settings of DNN. U_{x_U} showed similar tendencies in artificial datasets reconstruction to those in flume experiment reconstruction, but deviation of U_{x_U} was so large for U_{x_U} in flume experiment reconstruction that it seems unlikely to have originated solely from the DNN model. The tendencies of deviation for C_i in reconstruction of flume experiment datasets did not match those for artificial datasets, thus it also did not occur due to tendencies of the inverse model.

(2) For C_i, the source of deviation may be inaccuracies in measurements. Due to instabilities of flow during experiments, measurements conducted with great difficulty while the experiments were running. As shown in Figure 7, sampled concentrations of some measured C_i were extremely small ($< 0.05\%$), making it susceptible to minor disturbances during sampling and measurements. For values that are extremely small, even minor deviations appears to be large. Thus for C_i, the main source of deviation may not be the reconstructed values but the measured values.

(3) As U_{x_U}, inaccuracy in the forward model in describing the physical processes of turbidity currents main be the main reason of deviation. There are several potential reasons to why the reconstruction of flow velocity did not go as well as the other parameters, but the most probable reason is inaccuracy of the entrainment function in describing the actual effect of entrainment in flow, considering that the exponent in the calculation of dimensionless vertical velocity in the entrainment function was

549 determine purely by optimization and differs greatly in previous studies (Parker et al.,
550 1987; Garcia & Parker, 1991; Dorrell et al., 2018). Another problem may lie in the layer
551 averaging of flow velocity. Even though the model uses layer averaged flow velocity
552 for calculation, it had been pointed out in recent research by (Luchi et al., 2018) that
553 a two layer model is more suitable for calculation of turbidity currents. This research
554 aims to verify DNN as a method of inverse analysis of turbidity currents. Improvement
555 of the forward model, including entrainment function and velocity calculation, should
556 be the next step in the inverse analysis study of turbidity currents.

557 6.3 Comparison of DNN with Existing Methodologies

558 In comparison to the previous methods of inverse analysis of turbidity currents,
559 the inversion method using DNN holds great advantage in calculation cost and the
560 accuracy of reconstruction. Previous inversion methods of turbidity currents seek
561 to optimize the initial conditions to a particular set of data collected from turbidite,
562 which is extremely time-consuming to apply to one dataset and does not guarantee the
563 general applicability of the method to turbidites (Lesshafft & Marquet, 2010; Parkin-
564 son et al., 2017; Nakao & Naruse, 2017). For example, genetic algorithm applied in
565 Nakao and Naruse (2017) initializes with a population of parameters and optimize
566 the population of parameters through selection and mutation, so that the eventual
567 parameters left can successfully reconstruct the target turbidite. However, each epoch
568 of optimization requires results of selection of the previous epoch, so that calculation
569 of the forward model cannot be parallelized over epochs. In adjoint method used in
570 Parkinson et al. (2017), control variables within the forward model of turbidity cur-
571 rents are first initialized and inputted into the numerical model. The turbidite deposit
572 profile is calculated and compared with the target values using a cost function, and
573 gradients of the cost function (objective function) for control variables are calculated
574 analytically. If the result is decided to be less than optimal, the adjoint model will
575 be run and control variables will be adjusted by descent method. Adjusted control
576 variables will again be inputted into the numerical model. This cycle is repeated until
577 the reconstructed deposit profile is judged to be optimal, and thus the iteration of
578 calculation cannot be performed simultaneously. In contrast, DNN finds out the gen-
579 eral functional relationship between the turbidite deposited and the current, making
580 it applicable to turbidity currents in general. Forward model calculation to produce
581 training data sets can be perfectly parallelized so that the amount of time need for
582 calculation reduces greatly.

583 Parallelization of the forward model calculation enables employment of the for-
584 ward model that is accurate and realistic. As a result, forward model used in this
585 research is much better at capturing the spatio-temporal evolution of turbidity cur-
586 rent in comparison to forward model used in previous research (Falcini et al., 2009;
587 Parkinson et al., 2017). Falcini et al. (2009) used a steady flow forward model, while
588 our forward model is a non-steady flow model that reproduces the evolution of flow over
589 time. Method implemented in Parkinson et al. (2017) omitted the effect of entrain-
590 ment, a significant part of sediment transport in flow. As a result, their reconstructed
591 values of flow height, concentration, and grain diameter of the turbidite were 2.56 km,
592 0.0494 %, and 103 μm, respectively (Parkinson et al., 2017). These values are largely
593 off the expected range when examined based on the objective values collected from the
594 turbidite deposits. In contrast, our predictions lie relatively close to the original values
595 collected. Our forward model on the other hand incorporates the effect of sediment
596 suspension. Another improvement from previous research is that forward model used
597 in this case applies to turbidity currents data of multiple grain-size classes.

598 In contrast, Lesshafft and Marquet (2010) proposed a method based on direct
599 numerical simulation (DNS) of the Navier-Stokes equations. However, the calculation
600 costs of the method are extremely high, making it unrealistic to apply the method

to natural scale turbidite. The computational cost of DNS is scaled to Re^3, thus limiting the effectiveness of DNS to only experimental scale flows (Biegert et al., 2017). As a result, the maximum value of Reynolds number attained in previous numerical simulation using DNS was 15,000 (Cantero et al., 2007), which corresponds to 3.0 cm/s for velocity and 50 cm for flow height. Thus, application of their methodology cannot be expected for turbidites in natural scales.

7 Conclusion

A new method for the inverse analysis of turbidite using DNN was verified with actual flume experiment data in this research. DNN proved to be an efficient method for inversion of turbidity currents without sacrificing the accuracy of reconstruction in comparison to previous methods. Verification with artificial datasets proved to perform well judging by the standard deviation, standard error and bias of the seven parameters reconstructed. In terms of application of DNN to experiment data, deposit profiles were well reconstructed but the initial flow conditions do not match the measured values perfectly.

The reconstructed flow height H for PP1 and PP2 were 0.129 m and 0.156 m, where are good matches with the measured values 0.116 m and 0.123 m. H reconstructed for BS1, BS2 and BS3 were 0.0717 m, 0.117 m, 0.149 m and H measured were 0.115 m, 0.209 m, 0.199 m, which have a larger difference than PP1 and PP2 but are still reasonable. H was underestimated for BS1, BS2 and BS3. T_d was underestimated for all experiments. For BS1, BS2 and BS3 the reconstructed values were 120 s, 187 s, 120s, and measured values were 411 s, 362 s, 233 s. For PP1 and PP2, the reconstructed values were 622 s and 731 s and the measured values were 936 s and 966 s. U was overestimated for all experiments, with PP1 and PP2 better reconstructed than BS1, BS2 and BS3. The reconstructed U for PP1 and PP2 were 0.136 m/s and 0.121 m/s and measured values were 0.0608 m/s and 0.0923 m/s. The reconstructed U for BS1, BS2 and BS3 were 0.236 m/s, 0.324 m/s and 0.348 m/s and measured values were 0.0831 m/s, 0.142 m/s and 0.113 m/s.

Overall DNN showed good performance for inversion of artificial datasets and some parameters of the experiment data. As discussed in Section 6.2, the deposit profiles were well reconstructed, indicating success of DNN in the exploration of the functional relationship between initial conditions of flow and resulting deposits. Results of verification with artificial datasets and flume experiments show that the current forward model implemented is competent in performing inversion on turbidity currents, but need to be more robust for application to a wide range of flow conditions. Improvement of forward models and parameters such as the entrainment function will be the top priority in the future. Hyperparameter settings and internal structure of DNN also have room for improvement judging from the inversion result of artificial datasets. Application of DNN to field datasets will be the eventual goal in the future.

Appendix A Details of Forward Model Implemented

A1 Example of Forward Model Calculation

The forward model was tested with two sets of numerical simulations of turbidity currents. Testing was conducted using the forward model programmed for the production of artificial datasets of plastic particle only experiments. The settings of the numerical simulations are shown in Table A1. The time evolution of the high $C_{\mathrm{T},0}$, U_0 simulation is shown in Figure A1 and the time evolution of the low $C_{\mathrm{T},0}$, U_0 simulation is shown in Figure A2. In both cases, flow height H was greater toward the head of the current. H at the head of the current also grew over time (Figures A1A and A2A). Flow velocity U in the high $C_{\mathrm{T},0}$, U_0 simulation increased when the current prop-

agated downstream (Figure A1B), while U in the low $C_{\mathrm{T},0}$, U_0 simulation increased initially then decreased as the current propagated (Figure A2B). Total volumetric concentration of sediment C_{T} in flow decreased downstream both cases (Figures A1C and A2C). In the high $C_{\mathrm{T},0}$, U_0 case, a larger portion of sediment was deposited downstream than the low $C_{\mathrm{T},0}$, U_0 case (Figures A1D and A2D). The low $C_{\mathrm{T},0}$, U_0 case had most sediment deposited toward the upstream end of flow.

For the high $C_{\mathrm{T},0}$, U_0 simulation, a thicker deposit was observed for grain-size class 1 than for grain-size classes 3 and 4 (Figures A1E,G,H). Even though the initial concentrations of the finer grain-size classes 3 and 4 $C_{3,0}$, $C_{4,0}$ were higher than that of the coarser grain-size class 1 ($C_{1,0}$), less fine sediment was deposited since it was more likely to stay suspended and be carried beyond the lower flow boundary by the high-velocity flow. For the low $C_{\mathrm{T},0}$, U_0 simulation, the grain-size class with a thicker deposit has a higher initial concentration. The coarsest grain-size class, grain-size class 1, had almost all sediment deposited near the upstream boundary, while the finest grain-size class, grain-size class 4, had sediment spread out toward the downstream direction (Figures A2E,H). This happened because the low-velocity flow was unable to keep coarse sediment suspended.

Table A1. Initial flow conditions of numerical simulations of turbidity currents.

	High $C_{\mathrm{T},0}$, U_0	Low $C_{\mathrm{T},0}$, U_0
H_0 (m)	0.15	0.15
U_0 (m/s)	0.3	0.03
$C_{\mathrm{T},0}$	0.06	0.005
$C_{1,0}$	0.01	0.00025
$C_{2,0}$	0.02	0.0025
$C_{3,0}$	0.018	0.00175
$C_{4,0}$	0.012	0.0005
c_{f}	0.002	0.002
r_{o}	1.5	1.5
Duration (s)	420	420

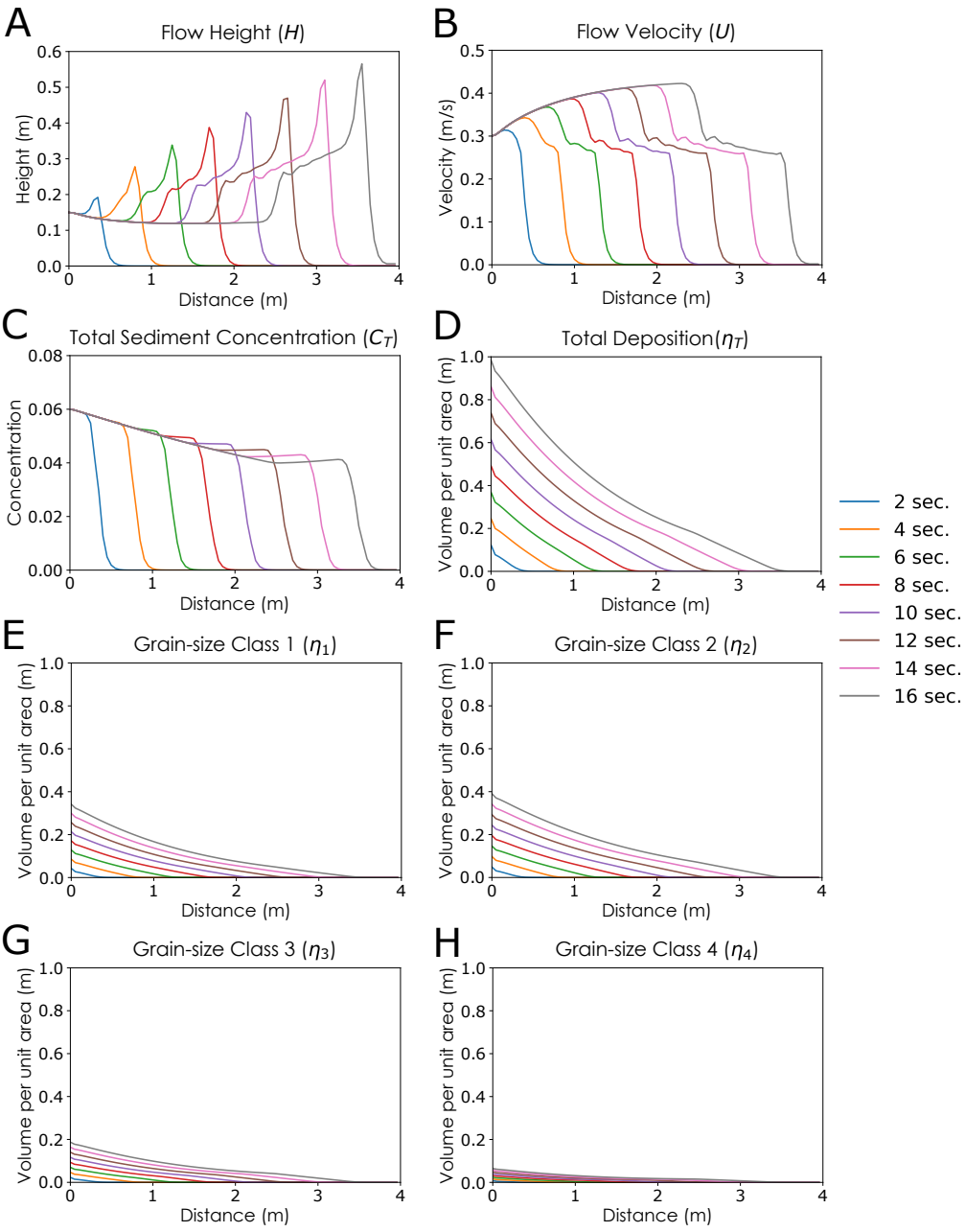

Figure A1. Example of forward model calculation with high initial flow velocity and sediment concentration (Table A1). A. Time evolution of flow height H. B. Time evolution of flow velocity U. C. Time evolution of total sediment volumetric concentration C_{T}. D. Time evolution of deposit profile η_{T}. E. Time evolution deposit profile of grain-size class 1 η_1. F. Time evolution of deposit profile of grain-size class 2 η_1. G. Time evolution of deposit profile of grain-size class 3 η_1. H. Time evolution of deposit profile of grain-size class 4 η_1.

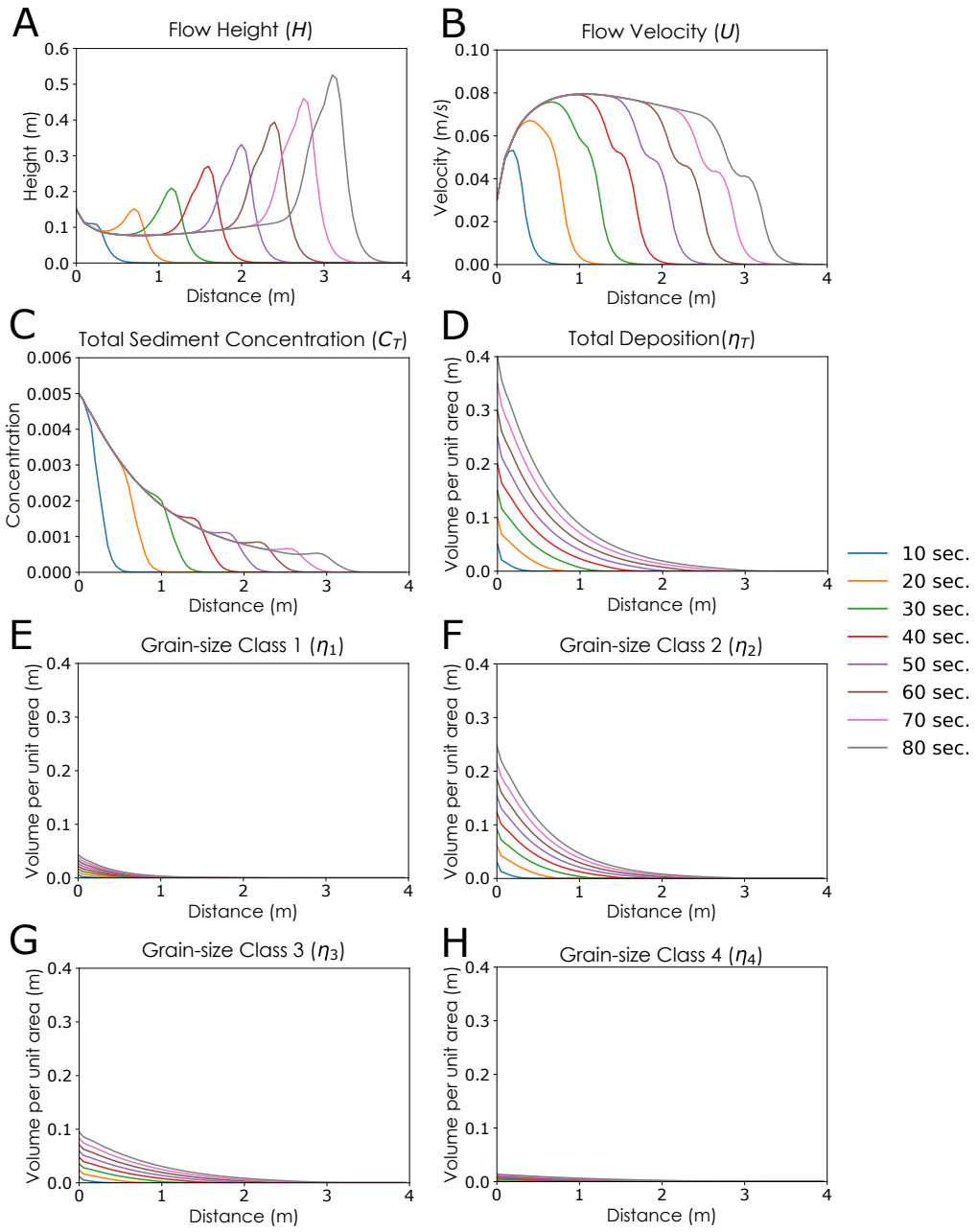

Figure A2. Example of forward model calculation with low initial flow velocity and sediment concentration (Table A1). A. Time evolution of flow height H. B. Time evolution of flow velocity U. C. Time evolution of total sediment volumetric concentration C_{T}. D. Time evolution of deposit profile η_{T}. E. Time evolution deposit profile of grain-size class 1 η_1. F. Time evolution of deposit profile of grain-size class 2 η_1. G. Time evolution of deposit profile of grain-size class 3 η_1. H. Time evolution of deposit profile of grain-size class 4 η_1.

667 ## A2 Sensitivity Tests of Forward Model

668 The degree of sensitivity of the forward model against change in the initial con-
669 ditions of the flow and the model parameters was tested (Table A2). Testing was con-
670 ducted using the forward model programmed for the production of artificial datasets
671 of plastic particle only experiments. Numerical simulations were conducted with dif-
672 ferent values of the six parameters H_0, U_0, $C_{\mathrm{T},0}$, e_s, r_o, c_f. Other parameters were
673 unchanged for the simulations.

674 The results of the sensitivity tests showed that change in deposit profile occurs
675 when initial flow conditions differ (Figure A3). The volume of sediment deposited
676 increased overall as H_0 increased (Figure A3A). Same trend was observed for U_0, and
677 $C_{\mathrm{T},0}$ (Figure A3B, C). Out of these three parameters, the amount of increase in deposit
678 thickness was greatest for $C_{\mathrm{T},0}$, and smallest for U_0. With regard to model closure
679 parameters, the resultant deposit profile showed nearly no change for different en-
680 trainment coefficient e_s (Figure A3D). Slight lower amount of deposition was observed
681 for greater e_s. An increase in the amount of deposition was observed as c_f decreases
682 (Figure A3F). The thickness of deposit increased moderately when r_o increased.

Table A2. Settings for sensitivity tests of forward model.

Case	H_0 (m)	U_0 (m/s)	$C_{\mathrm{T},0}$	e_s	r_o	c_f
1	0.15	0.15	0.03	GP	1.5	0.002
2	0.3	0.15	0.03	GP	1.5	0.002
3	0.05	0.15	0.03	GP	1.5	0.002
4	0.15	0.3	0.03	GP	1.5	0.002
5	0.15	0.05	0.03	GP	1.5	0.002
6	0.15	0.15	0.06	GP	1.5	0.002
7	0.15	0.15	0.005	GP	1.5	0.002
8	0.15	0.15	0.03	GPx2	1.5	0.002
9	0.15	0.15	0.03	GPx0.5	1.5	0.002
10	0.15	0.15	0.03	GP	2.0	0.002
11	0.15	0.15	0.03	GP	1.0	0.002
12	0.15	0.15	0.03	GP	1.5	0.01
13	0.15	0.15	0.03	GP	1.5	0.004
14	0.15	0.15	0.03	GP	1.5	0.001
15	0.15	0.15	0.03	GP	1.5	0.0005

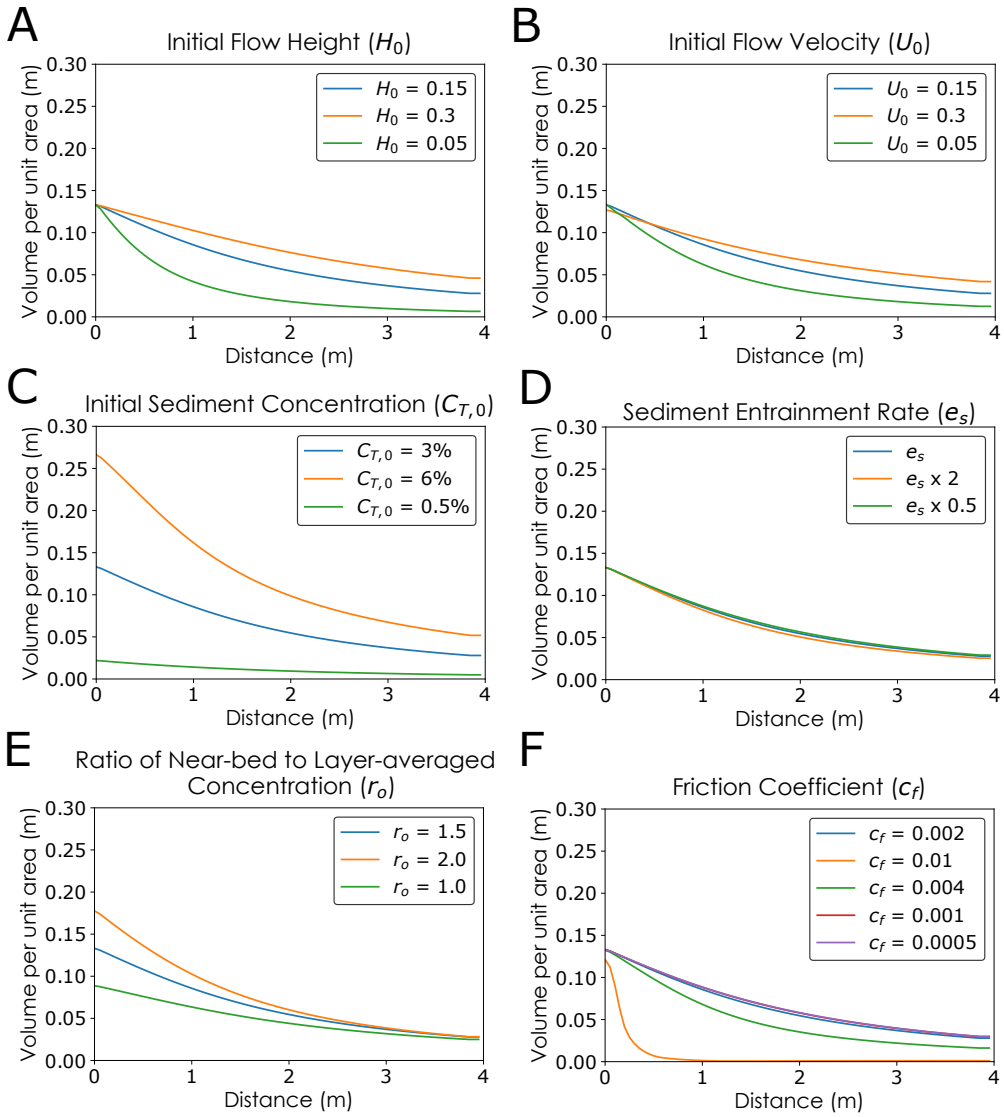

Figure A3. Sensitivity tests of deposit profile of artificial turbidites against change in initial flow conditions and closure parameters (Table A2). A. Dependency on initial flow height H_0. B. Dependency on initial flow velocity U_0. C. Dependency on initial total sediment volumetric concentration $C_{T,0}$. D. Dependency on sediment entrainment rate e_s. E. Dependency on ratio of near-bed to layer-averaged concentration r_o. F. Dependency on friction coefficient c_f.

Notation

$\boldsymbol{\alpha_1}$, $\boldsymbol{\alpha_2}$ Parameters related to sediment entrainment
$\boldsymbol{c_f}$ Friction coefficient
$\boldsymbol{C_i}$ Layer-averaged volumetric concentration of suspended sediment of the ith grain-size class
$\boldsymbol{C_T}$ Layer-averaged total concentration of suspended sediment
$\boldsymbol{D_i}$ Representative grain diameter of the ith grain-size class
$\boldsymbol{e_{si}}$ Entrainment rate of sediment of the ith grain-size class into suspension
$\boldsymbol{e_w}$ Entrainment rate of ambient water to flow
$\boldsymbol{F_i}$ Volume fraction of the ith grain-size class in active layer
$\boldsymbol{g}$ gravitational acceleration
$\boldsymbol{H}$ Flow height
$\boldsymbol{L_a}$ Active layer thickness
$\boldsymbol{R}$ Submerged specific density of sediment
$\boldsymbol{R_{fi}}$ Dimensionless particle fall velocity of the ith grain-size class
$\boldsymbol{Re_{pi}}$ Particle Reynolds number of the ith grain-size class
$\boldsymbol{r_o}$ Ratio of near-bed suspended sediment concentration to the layer-averaged concentration of suspended sediment
$\boldsymbol{S}$ Slope gradient
$\boldsymbol{S_f}$ Friction slope
$\boldsymbol{t}$ Time
$\boldsymbol{T_d}$ Flow duration
$\boldsymbol{U}$ Layer-averaged flow velocity
$\boldsymbol{u_*}$ Shear velocity
$\boldsymbol{w_i}$ Settling velocity of a sediment particle of the ith grain-size class
$\boldsymbol{x}$ Streamwise distance
$\boldsymbol{\eta_i}$ Volume per unit area of bed sediment of the ith grain-size class
$\boldsymbol{\eta_T}$ Total volume per unit area of bed sediment
$\boldsymbol{\kappa}$ Parameter related to artificial viscosity
$\boldsymbol{\lambda_p}$ Porosity of bed sediment
$\boldsymbol{\mu}$ Dynamic viscosity of water
$\boldsymbol{\nu}$ Kinematic viscosity of water
$\boldsymbol{\rho}$ Density of water

Acknowledgments

This work was supported by the Sediment Dynamics Research Consortium (SDRC). DOI for data and code is 10.5281/zenodo.3765813.

References

Abadi, M., Agarwal, A., Barham, P., Brevdo, E., Chen, Z., Citro, C., ... Zheng, X. (2015). *TensorFlow: Large-scale machine learning on heterogeneous systems.* Retrieved from `http://tensorflow.org/` (Software available from tensorflow.org)

Altinakar, M., Graf, W., & Hopfinger, E. (1996). Flow structure in turbidity currents. *Journal of Hydraulic Research*, *34*(5), 713-718. Retrieved from `https://doi.org/10.1080/00221689609498467` doi: 10.1080/00221689609498467

Arai, K., Naruse, H., Miura, R., Kawamura, K., Hino, R., Ito, Y., ... Kasaya, T. (2013, 11). Tsunami-generated turbidity current of the 2011 tohoku-oki earthquake. *Geology*, *41*(11), 1195–1198.

Baas, J. H., Van Dam, R. L., & Storms, J. E. A. (2000). Duration of deposition from decelerating high-density turbidity currents. *Sedimentary Geology*, *136*(1), 71–88.

Biegert, E., Vowinckel, B., Ouillon, R., & Meiburg, E. (2017). High-resolution simulations of turbidity currents. *Progress in Earth and Planetary Science*, *4*(1), 33.

Bottou, L. (2010). Large-scale machine learning with stochastic gradient descent. In Y. Lechevallier & G. Saporta (Eds.), *Proceedings of compstat'2010* (pp. 177–186). Heidelberg: Physica-Verlag HD.

Bouma, A. H. (1962). *Sedimentology of some flysch deposits: A graphic approach to facies interpretation*. Elsevier.

Cantero, M. I., Balachandar, S., & Garcia, M. H. (2007). High-resolution simulations of cylindrical density currents. *Journal of Fluid Mechanics*, *590*, 437–469.

Daly, R. A. (1936). Origin of submarine canyons. *American Journal of Science*, *31*(186), 401–420.

Davison, A. C., & Hinkley, D. V. (1997). *Bootstrap methods and their application*. Cambridge University Press. doi: 10.1017/CBO9780511802843

Dietrich, W. E. (1982). Settling velocity of natural particles. *Water Resources Research*, *18*(6), 1615–1626. doi: 10.1029/WR018i006p01615

Dorrell, R. M., Amy, L. A., Peakall, J., & McCaffrey, W. D. (2018). Particle size distribution controls the threshold between net sediment erosion and deposition in suspended load dominated flows. *Geophysical Research Letters*, *45*(3), 1443-1452.

Falcini, F., Marini, M., Milli, S., & Moscatelli, M. (2009). An inverse problem to infer paleoflow conditions from turbidites. *Journal of Geophysical Research: Oceans*, *114*.

Fukushima, Y., Parker, G., & Pantin, H. M. (1985). Prediction of ignitive turbidity currents in scripps submarine canyon. *Marine Geology*, *67*(1), 55–81.

Garcia, M., & Parker, G. (1991). Entrainment of bed sediment into suspension. *Journal of Hydraulic Engineering*, *117*(4), 414-435.

Garcia, M., & Parker, G. (1993). Experiments on the entrainment of sediment into suspension by a dense bottom current. *Journal of Geophysical Research*, *98*(C3), 4793–4807.

Gibbs, R. J. (1974). A settling tube system for sand-size analysis. *Journal of Sedimentary Petrology*, *44*(2), 583–588.

Jameson, A., Schmidt, W., & Turkel, E. (1981). Numerical solution of the euler equations by finite volume methods using runge kutta time stepping schemes. In *14th fluid and plasma dynamics conference* (p. 1259).

Johnson, D. W. (1939). *The origin of submarine canyons: A critical review of hypotheses*. Columbia University Press.

Kostic, S., & Parker, G. (2006). The response of turbidity currents to a canyon–fan transition: Internal hydraulic jumps and depositional signatures. *Journal of Hydraulic Research*, *44*(5), 631–653. Retrieved from `https://doi.org/10.1080/00221686.2006.9521713` doi: 10.1080/00221686.2006.9521713

Krizhevsky, A., Sutskever, I., & Hinton, G. E. (2012). Imagenet classification with deep convolutional neural networks. In F. Pereira, C. J. C. Burges, L. Bottou, & K. Q. Weinberger (Eds.), *Advances in neural information processing systems 25* (pp. 1097–1105). Curran Associates, Inc. Retrieved from `http://papers.nips.cc/paper/4824-imagenet-classification-with-deep-convolutional-neural-networks.pdf`

Kuenen, P. H., & Migliorini, C. I. (1950). Turbidity currents as a cause of graded bedding. *The Journal of Geology*, *58*(2), 91–127.

Lesshafft, L., & Marquet, O. (2010). Optimal velocity and density profiles for the onset of absolute instability in jets. *Journal of Fluid Mechanics*, *662*, 398–408.

Liang, S., & Srikant, R. (2016). Why deep neural networks for function approxima-

tion? *CoRR, abs/1610.04161*. Retrieved from http://arxiv.org/abs/1610.04161

Luchi, R., Balachandar, S., Seminara, G., & Parker, G. (2018). Turbidity currents with equilibrium basal driving layers: A mechanism for long runout. *Geophysical Research Letters*, *45*(3), 1518-1526. Retrieved from https://agupubs.onlinelibrary.wiley.com/doi/abs/10.1002/2017GL075608 doi: 10.1002/2017GL075608

Nakao, K., & Naruse, H. (2017, 12). Inverse analysis to reconstruct hydraulic conditions of non-steady turbidity currents based on multiple grain-size classes. *EarthArXiv*.

Naruse, H. (2005). Usage and advantages of an application program "stube" for settling tube grain-size analysis. *Journal of the Sedimentological Society of Japan*, *62*(62), 55–61.

Naruse, H., & Nakao, K. (2017, 12). Inverse analysis of turbidites by machine learning. *AGU Fall Meeting Abstracts*.

Naruse, H., & Olariu, C. (2008). Hydraulic conditions of turbidity currents estimated by inverse analysis. In *Fourth international conference on scour and erosion* (pp. 591–593). Japanese Geotechnical Society.

Nielsen, M. A. (2015). *Neural networks and deep learning*. Determination Press.

Parker, G., Garcia, M., Fukushima, Y., & Yu, W. (1987). Experiments on turbidity currents over an erodible bed. *Journal of Hydraulic Research*, *25*(1), 123–147.

Parkinson, S. D., Funke, S. W., Hill, J., Piggott, M. D., & Allison, P. A. (2017). Application of the adjoint approach to optimise the initial conditions of a turbidity current with the adjointturbidity 1.0 model. *Geoscientific Model Development*, *10*(3), 1051–1068.

Paull, C. K., Talling, P. J., Maier, K. L., Parsons, D., Xu, J., Caress, D. W., ... Cartigny, M. J. (2018). Powerful turbidity currents driven by dense basal layers. *Nature Communications*, *9*(1), 4114.

Pradhan, B., Lee, S., & Buchroithner, M. F. (2010). A gis-based back-propagation neural network model and its cross-application and validation for landslide susceptibility analyses. *Computers, Environment and Urban Systems*, *34*(3), 216–235.

Rogers, S. J., Fang, J. H., Karr, C. L., & Stanley, D. A. (1992). Determination of lithology from well logs using a neural network. *AAPG Bulletin*, *76*(5), 731–739.

Ruder, S. (2016). An overview of gradient descent optimization algorithms. *CoRR*, *abs/1609.04747*. Retrieved from http://arxiv.org/abs/1609.04747

Rumble, J. R. (2018). *Crc handbook of chemistry and physics, 99th edition*. CRC Press.

Schmidhuber, J. (2015). Deep learning in neural networks: An overview. *Neural Networks*, *61*, 85–117. Retrieved from http://www.sciencedirect.com/science/article/pii/S0893608014002135 doi: https://doi.org/10.1016/j.neunet.2014.09.003

Talling, P. J., Allin, J., Armitage, D. A., Arnott, R. W. C., Cartigny, M. J. B., Clare, M. A., ... Xu, J. (2015). Key future directions for research on turbidity currents and their deposits. *Journal of Sedimentary Research*, *85*(2), 153–169.

Talling, P. J., Amy, L. A., & Wynn, R. B. (2007). New insight into the evolution of large-volume turbidity currents: Comparison of turbidite shape and previous modelling results. *Sedimentology*, *54*(4), 737–769.

Talling, P. J., Masson, D. G., Sumner, E. J., & Malgesini, G. (2012). Subaqueous sediment density flows: Depositional processes and deposit types. *Sedimentology*, *59*(7), 1937–2003.

Vangriesheim, A., Khripounoff, A., & Crassous, P. (2009). Turbidity events observed in situ along the congo submarine channel. *Deep Sea Research Part II: Topical Studies in Oceanography*, *56*(23), 2208–2222.

Wang, Z., & Bovik, A. C. (2009). Mean squared error: Love it or leave it? a new look at signal fidelity measures. *IEEE Signal Processing Magazine*, *26*(1), 98–117. doi: 10.1109/MSP.2008.930649

Weimer, P., & Slatt, R. M. (2007). Introduction to the petroleum geology of deepwater settings. *AAPG Studies in Geology*, *57*, 149-227.

Wright, S., & Parker, G. (2004). Flow resistance and suspended load in sand-bed rivers: Simplified stratification model. *Journal of Hydraulic Engineering*, *130*(8), 796–805.

Xu, J. P., Noble, M. A., & Rosenfeld, L. K. (2004). In-situ measurements of velocity structure within turbidity currents. *Geophysical Research Letters*, *31*(9).

Yabe, T., Xiao, F., & Utsumi, T. (2001). The constrained interpolation profile method for multiphase analysis. *Journal of Computational Physics*, *169*(2), 556–593.